

AN EFFICIENT THRESHOLD DYNAMICS METHOD FOR TOPOLOGY OPTIMIZATION FOR FLUIDS

HUANGXIN CHEN, HAITAO LENG, DONG WANG, AND XIAO-PING WANG

ABSTRACT. We propose an efficient threshold dynamics method for topology optimization for fluids modeled with the Stokes equation. The proposed algorithm is based on minimization of an objective energy function that consists of the dissipation power in the fluid and the perimeter approximated by nonlocal energy, subject to a fluid volume constraint and the incompressibility condition. We show that the minimization problem can be solved with an iterative scheme in which the Stokes equation is approximated by a Brinkman equation. The indicator functions of the fluid-solid regions are then updated according to simple convolutions followed by a thresholding step. We prove mathematically that the iterative algorithm has the total energy decaying property. The proposed algorithm is simple and easy to implement. Extensive numerical experiments in both two and three dimensions show that the proposed iteration algorithm converges in much fewer iterations and is more efficient than many existing methods. In addition, the numerical results show that the algorithm is very robust and insensitive to the initial guess and the parameters in the model.

1. INTRODUCTION

Topology optimization in fluid mechanics has become a significant problem due to its application in many industrial problems such as the optimization of transport vehicles and biomechanical structure. The process of topology optimization allows the introduction of new boundaries as part of the solution and is thus more flexible than shape optimization, which requires that the topology be predetermined. The method of topology optimization was originally developed for the optimal design in structural mechanics [9, 10] and has been applied in a variety of physical fields such as acoustics, electromagnetics, fluid flow, and thermal problems [10, 12, 17, 19, 42, 56]. Topology optimization was first applied to fluid mechanics by Borrvall and Petersson [12] by adopting the concept of density methods to Stokes flows. In [12], the domain with fluid-solid regions was treated as the porous medium, the Brinkman flow was introduced to obtain a well-posed problem to minimize the total dissipation power, and the discrete optimization problem was further solved with the method of moving asymptotes (MMA) [59] to obtain the optimal designed regions for fluids and solids. Topology optimization in fluid mechanics has since been extended to the Darcy-Stokes flow model [30, 67], Navier-Stokes flow [18, 25, 27, 45, 62, 72], and non-Newtonian flow [50], and it has also been applied in the design of more complicated fluidic devices [6, 43, 44].

It is since the original work by Bendsøe and Kikuchi [10] on homogenization approach to topology optimization that many methods has been developed: density interpolation [8, 73]; level-set method approach [5]; topological derivatives [58] [57] (and the reference therein); phase field method [13] [25]; evolutionary structural optimization (ESO) approaches [68], the bi-directional schemes (BESO) [71]; and several others. The level set based approach [46] has been very popular in topology optimization. It was applied to fluidic topology optimization (cf. [14, 33, 62, 72] and the references therein) where the fluid-solid interface is described by the zero-level contour of a level set function. In [2], the authors proposed a method that combines the sensitivity analysis and the level set method for many problems in topology optimization. It has been subsequently extended to multi-phase structure optimization [3], optimal design [4], multiple loads structural optimization [5], and also fluid problems [33, 62].

2010 *Mathematics Subject Classification.* 35K93, 35K05, 65M12, 35Q35, 49Q10, 65M60, 76S05.

Key words and phrases. Topology optimization, Stokes flow, threshold dynamics method, mixed finite-element method, convolution, fast Fourier transform.

This research was supported in part by the Hong Kong Research Grants Council (GRF grants 16302715, 16324416, 16303318, and NSFC-RGC joint research grant N-HKUST620/15). H. Chen and D. Wang acknowledge the hospitality of the Department of Mathematics at the Hong Kong University of Science and Technology during their visit. The work of H. Chen was supported by the NSF of China (Grant No. 11771363, 91630204, 51661135011), the Fundamental Research Funds for the Central Universities (Grant No. 20720180003), and the Program for Prominent Young Talents in Fujian Province University.

To ensure well-posedness and mesh-independent solutions, regularization is usually needed in topology optimization. Many robust regularization approaches were introduced. For example, regularizing the optimization problem by introducing fictitious interface energy [70] or penalizing the original objective function by perimeter control functions based on phase field method [51]. The level set based method without additional regularization can also be applied to solve topology optimization problems (e.g. [49] and the reference therein).

The threshold dynamics method developed by Merriman, Bence, and Osher (MBO) [38–40] is an efficient method for simulating the motion of the interface driven by the mean curvature. The method alternatively diffuses characteristic functions of regions and sharpens through thresholding to generate the interface motion implicitly. To be precise, let D be domain of one phase with boundary $\Gamma = \partial D$ that separating phases. The domain D and boundary Γ are updated via two steps:

Step 1: Solve free space heat equation with initially constant temperature in domain D and zero elsewhere in a short time τ by convolution with heat kernel,

$$\phi(x) = G_\tau * \chi_D,$$

where χ_D is the characteristic function of D . Here,

$$G_\tau = \frac{1}{(4\pi\tau)^{d/2}} \exp\left(-\frac{|x|^2}{4\tau}\right),$$

is the heat kernel where d is spacial dimension of D .

Step 2: Obtain new domain D^* and interface $\Gamma^* = \partial D^*$ by thresholding,

$$D^* = \{x : \phi(x) \geq \frac{1}{2}\}.$$

The convergence of this algorithm to mean curvature flow was well established [7, 15, 24, 60].

Esedoglu and Otto [21] gave a variational formulation for the method and generalized it to multiphase problems with arbitrary surface tensions. They observed that,

$$(1.1) \quad J_\tau(D) = \sqrt{\frac{\pi}{\tau}} \int \chi_{D^c} G_\tau * \chi_D \, dx$$

is a non-local approximation to perimeter of boundary of D and showed that threshold dynamics scheme dissipates this functional J_τ at each iteration. Moreover, they gave the following minimizing movement interpretation:

$$D^* = \arg \min_{\bar{D}} J_\tau(\bar{D}) + g(\chi_{\bar{D}} - \chi_D),$$

where

$$g(a) = \sqrt{\frac{\pi}{\tau}} \int a G_\tau * a \, dx = \sqrt{\frac{\pi}{\tau}} \int [G_{\tau/2} * a]^2 \, dx$$

is a positive definite quadratic functional measuring the distance between \bar{D} and D . Essentially, the threshold dynamics method is reformulated into an iterative method for domain optimization problem with the non-local interface energy $J_\tau(D)$ as the objective function and the admissible set being the characteristic functions of domain D . The method has attracted considerable attention due to its simplicity and unconditional stability. It has since been extended to deal with many other applications, including the problem of area-preserving or volume-preserving interface motion [55], image processing [23, 37, 64], problems of anisotropic interface motion [11, 20, 41, 54], the wetting problem on solid surfaces [69], the generation of quadrilateral meshes [61], graph partitioning and data clustering [26], and auction dynamics [32]. Various algorithms and rigorous error analysis have been introduced to refine and extend the original MBO method and related methods for these problems (see, e.g., [22, 31, 40, 52, 53, 63]). Adaptive methods have also been used to accelerate this type of method [34] based on nonuniform fast Fourier transform. Laux et al. [35, 36] rigorously proved the convergence of the method proposed by [21]. A generalized manifold-valued threshold dynamics method was developed by [47, 48, 65].

In this paper, we generalize the threshold dynamics approach to the topology optimization for fluids. In our approach, the total energy (objective function) consists of the dissipation power in the fluid and the perimeter regularization, subject to a fluid volume constraint and the Stokes equation for the velocity field. The perimeter term is based on convolution of the heat kernel with the characteristic functions

of the fluid regions. The porous medium approach is used in our algorithm, and we introduce the Brinkman equation, which “interpolates” between the Stokes equation in the flow region and some Darcy flow through a porous medium (a weakened nonfluid region). We then solve the Brinkman equation for the whole domain by the standard mixed finite-element method and update the fluid-solid regions by convolution and with a simple thresholding step. In particular, the convolutions can be efficiently computed on a uniform grid by fast Fourier transform (FFT) with the an optimal complexity of $O(N \log N)$.

An efficient threshold dynamics scheme is derived to minimize an approximate total energy (objective function) with constraints. The main observation is that our objective function is concave with respect to the characteristic function of the domain when the state variable (velocity field) is fixed. This allows us to design an iterative method to minimize the objective function in a simple and robust way. The proposed method is easy to implement and numerical results show that the method is efficient, robust and insensitive to the initial guess and parameters. In particular, we further prove the unconditionally energy-decaying property of the proposed algorithm which is usually not theoretically guaranteed in level set based methods. Numerical results show that the number of iterations needed to reach the stationary state is greatly reduced when compared to some level set based method or the MMA. Furthermore, our method can be easily extended to cases with arbitrary numbers of phases in multi-phase topology optimization.

The paper is organized as follows. In Section 2, we show the mathematical model. In Section 3, we introduce an approximate energy to the total energy and derive an efficient threshold dynamics method. The unconditional stability of the threshold dynamics method (*i.e.*, the energy decaying property) is proved in Section 4. We discuss the numerical implementation in Section 5 and verify the efficiency and the energy decaying property of the algorithm in Section 6. We make conclusions, and discuss some ideas for future work in Section 7.

2. MATHEMATICAL MODEL

In this section, we consider the mathematical model for topology optimization for fluids in Stokes flow. Denote $\Omega \in \mathbb{R}^d$ ($d = 2, 3$) as the computational domain, which is fixed throughout optimization, and assume that Ω is a bounded Lipschitz domain with an outer unit normal \mathbf{n} such that $\mathbb{R}^d \setminus \bar{\Omega}$ is connected. Furthermore, we denote $\Omega_0 \subset \Omega$ as the domain of the fluid, which is a Caccioppoli set whose boundary is measurable and has a (at least locally) finite measure (cf. [29]), and $\Omega \setminus \Omega_0 \in \Omega$ as the solid domain. Throughout the paper, we use the standard notations and definitions for Sobolev spaces (cf. [1]). Our goal is to determine an optimal shape of Ω_0 that minimizes the following objective functional consisting of the total potential power and a perimeter regularization term,

$$(2.1) \quad \min_{(\Omega_0, \mathbf{u})} J_0(\Omega_0, \mathbf{u}) = \int_{\Omega} \left(\frac{\mu}{2} |D\mathbf{u}|^2 - \mathbf{u} \cdot \mathbf{f} \right) dx + \gamma |\Gamma|$$

subject to

$$(2.2a) \quad \nabla \cdot \mathbf{u} = 0, \quad \text{in } \Omega,$$

$$(2.2b) \quad \nabla p - \nabla \cdot (\mu \nabla \mathbf{u}) = \mathbf{f}, \quad \text{in } \Omega_0,$$

$$(2.2c) \quad \mathbf{u} = 0, \quad \text{in } \Omega \setminus \Omega_0,$$

$$(2.2d) \quad \mathbf{u}|_{\partial\Omega} = \mathbf{u}_D, \quad \text{on } \partial\Omega,$$

$$(2.2e) \quad |\Omega_0| = \beta |\Omega| \quad \text{with a fixed parameter } \beta \in (0, 1).$$

Here, $\mathbf{u} : \Omega \rightarrow \mathbb{R}^d$, $D\mathbf{u}$ is the distributional derivative of \mathbf{u} , μ is the dynamic viscosity of the fluid, p is the pressure, $\mathbf{u}_D : \partial\Omega \rightarrow \mathbb{R}^d$ is a given function, $\mathbf{f} : \Omega \rightarrow \mathbb{R}^d$ is a given external force, $|\Gamma|$ is the perimeter of the boundary of $\Gamma = \partial\Omega_0$, and $\gamma > 0$ is a weighting parameter.

3. DERIVATION OF THE ALGORITHM

In this section, we develop an efficient threshold dynamics method for the topology optimization problem discussed in (2.1) and (2.2) for fluids in Stokes flow. Note that the goal is to determine the optimal interface between liquid and solid that minimizes functional (2.1) subject to constraints (2.2). Motivated by the idea from the threshold dynamics methods developed by [21, 64, 66, 69], we use the indicator functions for the fluid region and the solid region to implicitly represent the interface.

3.1. Approximate energy. Define an admissible set \mathcal{B} as follows:

$$(3.1) \quad \mathcal{B} := \{(v_1, v_2) \in BV(\Omega) \mid v_i(x) = \{0, 1\}, v_1(x) + v_2(x) = 1 \text{ a.e. in } \Omega, \text{ and } \int_{\Omega} v_1 \, d\mathbf{x} = V_0\},$$

where $BV(\Omega)$ is the vector space of functions with bounded variation in Ω , and V_0 is the fixed volume of the fluid region. We introduce $\chi_1(\mathbf{x})$ to denote the indicator function of the fluid region Ω_0 , *i.e.*,

$$\chi_1(\mathbf{x}) := \begin{cases} 1, & \text{if } \mathbf{x} \in \Omega_0, \\ 0, & \text{otherwise,} \end{cases}$$

and $\chi_2(\mathbf{x})$ as the indicator function of $\Omega \setminus \Omega_0$, *i.e.*, $\chi_2(\mathbf{x}) = 1 - \chi_1(\mathbf{x})$. The interface Γ is then implicitly represented by χ_1 and χ_2 . Let $\chi = (\chi_1, \chi_2)$ and we have $\chi \in \mathcal{B}$. The perimeter of the interface Γ is then approximated by,

$$(3.2) \quad |\Gamma| \approx \sqrt{\frac{\pi}{\tau}} \int_{\Omega} \chi_1 G_{\tau} * \chi_2 \, d\mathbf{x},$$

where $G_{\tau}(\mathbf{x}) = \frac{1}{(4\pi\tau)^{\frac{d}{2}}} \exp\left(-\frac{|\mathbf{x}|^2}{4\tau}\right)$ is the Gaussian kernel (See [21] for more details on this approximation).

We solve the optimization problem (2.2) by iteration. At each iteration, one must solve the Stokes equation in the fluid domain, which is changing in the iteration. It is more convenient numerically to use the porous medium approach as in [16, 25]. The idea is to “interpolate” between the Stokes equation in the fluid domain (*i.e.*, $\{\mathbf{x} \mid \chi_1(\mathbf{x}) = 1\}$) and $\mathbf{u} = 0$ in the solid domain (*i.e.*, $\{\mathbf{x} \mid \chi_2(\mathbf{x}) = 1\}$) by introducing an additional penalization term,

$$(3.3a) \quad \nabla \cdot \mathbf{u} = 0, \text{ in } \Omega,$$

$$(3.3b) \quad \nabla p - \nabla \cdot (\mu \nabla \mathbf{u}) + \alpha(\mathbf{x})\mathbf{u} = \mathbf{f}, \text{ in } \Omega,$$

$$(3.3c) \quad \mathbf{u}|_{\partial\Omega} = \mathbf{u}_D, \text{ on } \partial\Omega.$$

Here, $\alpha(\mathbf{x})$ is a smooth function that varies between 0 and $\bar{\alpha}_{\tau}$ through a thin interface layer around Γ , and $\bar{\alpha}_{\tau}^{-1}$ is the permeability. In the current representation of the interface, we use the 0.5 level set of $\phi = G_{\tau} * \chi_2$ to approximate the position of the interface Γ . It is well known that such ϕ is a smooth function between $[0, 1]$ and admits a change from 0 to 1 in an $O(\sqrt{\tau})$ thin layer. Hence, α is given by

$$(3.4) \quad \alpha = \bar{\alpha}_{\tau} \phi = \bar{\alpha}_{\tau} G_{\tau} * \chi_2.$$

In the limiting model (*i.e.*, $\tau \searrow 0$), $\bar{\alpha}_{\tau}$ should be set as $+\infty$ to make the constraints $\{\mathbf{u} = 0 \text{ in } \Omega \setminus \Omega_0\}$ satisfy. Also, to ensure that the velocity vanishes outside the fluid domain when $\tau \searrow 0$, we add a penalty term

$$\int_{\Omega} \frac{\alpha}{2} |\mathbf{u}|^2 \, dx = \int_{\Omega} \frac{\bar{\alpha}_{\tau} G_{\tau} * \chi_2}{2} |\mathbf{u}|^2 \, dx$$

to the objective functional. In subsequent calculations, for numerical consideration, we fix $\bar{\alpha}_{\tau}$ as a sufficiently large constant, $\bar{\alpha}$. In this porous media approach, the system (3.3) is solved for a fixed domain Ω .

Finally, combining (2.1), (3.2), (3.4), and the penalty term, we arrive at the following approximate objective functional

$$(3.5) \quad J^{\tau}(\chi, \mathbf{u}) = \int_{\Omega} \left(\frac{\mu}{2} |D\mathbf{u}|^2 + \frac{\bar{\alpha}}{2} |\mathbf{u}|^2 G_{\tau} * \chi_2 - \mathbf{u} \cdot \mathbf{f} + \gamma \sqrt{\frac{\pi}{\tau}} \chi_1 G_{\tau} * \chi_2 \right) \, d\mathbf{x}.$$

Remark 3.1. For simplicity, we use the same τ in the second and the fourth terms of the above approximate energy. Indeed, one can also use different values of τ in the two terms and the property of the algorithm will be similar.

Now, we consider the following approximate formulation of the problem by

$$(3.6) \quad \min_{(\chi, \mathbf{u})} J^{\tau}(\chi, \mathbf{u}), \text{ subject to } \chi = (\chi_1, \chi_2) \in \mathcal{B} \text{ and } \mathbf{u} \text{ satisfies (3.3).}$$

In the following, we give the derivation of the threshold dynamics scheme to solve (3.6).

3.2. Derivation of the scheme. In this section, we use a coordinate descent algorithm to minimize the approximate energy (3.5) with constraints (3.3). A similar idea has been applied in the design of a threshold dynamics method of image segmentation [64]. Given an initial guess $\chi^0 = (\chi_1^0, \chi_2^0)$, we compute a series of minimizers

$$\mathbf{u}^0, \chi^1, \mathbf{u}^1, \chi^2, \dots, \mathbf{u}^k, \chi^{k+1}, \dots$$

such that

$$(3.7) \quad \mathbf{u}^k = \arg \min_{\mathbf{u} \in \mathcal{S}} J^\tau(\chi^k, \mathbf{u}),$$

$$(3.8) \quad \chi^{k+1} = \arg \min_{\chi \in \mathcal{B}} J^\tau(\chi, \mathbf{u}^k),$$

for $k = 0, 1, 2, \dots$. Here, the admissible set \mathcal{S} is defined as

$$\mathcal{S} := \{ \mathbf{u} \in H_{\mathbf{u}_D}^1(\Omega, \mathbb{R}^d) \mid \nabla \cdot \mathbf{u} = 0 \}$$

where $H_{\mathbf{u}_D}^1(\Omega, \mathbb{R}^d) = \{ \mathbf{u} \in H^1(\Omega, \mathbb{R}^d) \mid \mathbf{u}|_{\partial\Omega} = \mathbf{u}_D \}$, and \mathcal{B} is defined in (3.1).

Given the k -th iteration χ^k , we first solve (3.7) to get the \mathbf{u}^k . It is easy to see that the constraint minimization problem is equivalent to the following

$$\mathbf{u}^k = \arg \min_{\mathbf{u} \in H_{\mathbf{u}_D}^1(\Omega, \mathbb{R}^d)} J^\tau(\chi^k, \mathbf{u}) + \int_{\Omega} p \nabla \cdot \mathbf{u} \, d\mathbf{x}$$

with p as a Lagrangian multiplier. Variation of the above functional leads to the following Brinkman equation. That is, \mathbf{u}^k can be obtained by solving

$$(3.9) \quad \begin{cases} \nabla \cdot \mathbf{u} = 0, & \text{in } \Omega \\ \nabla p - \nabla \cdot (\mu \nabla \mathbf{u}) + \alpha^k \mathbf{u} = \mathbf{f}, & \text{in } \Omega \\ \mathbf{u}|_{\partial\Omega} = \mathbf{u}_D \end{cases}$$

where $\alpha^k = \frac{\bar{\alpha}}{2} G_\tau * \chi_2^k$. Because $J^\tau(\chi^k, \mathbf{u})$ is convex in \mathbf{u} , the solution (\mathbf{u}^k, p^k) of (3.9) is a minimizer of $J^\tau(\chi^k, \mathbf{u})$. The following lemma shows the existence of \mathbf{u} for the system (3.9) for a given $\chi \in \mathcal{B}$.

Lemma 3.1 ([25, 28]). *For every $\chi \in \mathcal{B}$, some $\mathbf{u} \in H_{\mathbf{u}_D}^1(\Omega, \mathbb{R}^d)$ exist that satisfy $\nabla \cdot \mathbf{u} = 0$ such that*

$$(3.10) \quad \int_{\Omega} \mu \nabla \mathbf{u} \cdot \nabla \mathbf{v} + \alpha \mathbf{u} \cdot \mathbf{v} \, d\mathbf{x} = \int_{\Omega} \mathbf{f} \cdot \mathbf{v} \, d\mathbf{x}, \quad \forall \mathbf{v} \in \mathbf{V},$$

where $\mathbf{V} := \{ \mathbf{v} \in H_0^1(\Omega, \mathbb{R}^d) \mid \nabla \cdot \mathbf{v} = 0 \}$.

Given \mathbf{u}^k , we now rewrite the objective functional $J^\tau(\chi, \mathbf{u})$ into $\tilde{J}^{\tau, k}(\chi)$ as follows:

$$(3.11) \quad \tilde{J}^{\tau, k}(\chi) := J^\tau(\chi, \mathbf{u}^k) = \int_{\Omega} \frac{\bar{\alpha}}{2} \chi_2 G_\tau * |\mathbf{u}^k|^2 \, d\mathbf{x} + \gamma \sqrt{\frac{\pi}{\tau}} \int_{\Omega} \chi_1 G_\tau * \chi_2 \, d\mathbf{x} + \int_{\Omega} \frac{\mu}{2} |D\mathbf{u}^k|^2 - \mathbf{u}^k \cdot \mathbf{f} \, d\mathbf{x}.$$

The next step is to find χ^{k+1} such that

$$(3.12) \quad \chi^{k+1} = \arg \min_{\chi \in \mathcal{B}} \tilde{J}^{\tau, k}(\chi).$$

It is the minimization of a concave functional on a nonconvex admissible set \mathcal{B} . However, we can relax it to a problem defined on a convex admissible set by finding r^{k+1} such that

$$(3.13) \quad r^{k+1} = \arg \min_{r \in \mathcal{H}} \tilde{J}^{\tau, k}(r),$$

where \mathcal{H} is the convex hull of \mathcal{B} defined as follows:

$$(3.14) \quad \mathcal{H} := \{ (v_1, v_2) \in BV(\Omega) \mid v_i(x) \in [0, 1], i = 1, 2, \text{ and } v_1(x) + v_2(x) = 1 \text{ a.e. in } \Omega, \int_{\Omega} v_1 \, d\mathbf{x} = V_0 \},$$

The following lemma shows that the relaxed problem (3.13) is equivalent to the original problem (3.12). Therefore, we can solve the relaxed problem (3.13) instead.

Lemma 3.2. *Let $\mathbf{u} \in H_{\mathbf{u}_D}^1(\Omega, \mathbb{R}^d)$ be a given function and $r = (r_1, r_2)$. Then*

$$(3.15) \quad \arg \min_{r \in \mathcal{H}} \tilde{J}^{\tau, k}(r) = \arg \min_{r \in \mathcal{B}} \tilde{J}^{\tau, k}(r).$$

Proof. Let $\tilde{r} = (\tilde{r}_1, \tilde{r}_2) \in \mathcal{H}$ be a minimizer of the functional $\tilde{J}^{\tau,k}(r)$ on \mathcal{H} . Because $\mathcal{B} \subset \mathcal{H}$, we have

$$\tilde{J}^{\tau,k}(\tilde{r}) = \min_{r \in \mathcal{H}} \tilde{J}^{\tau,k}(r) \leq \min_{r \in \mathcal{B}} \tilde{J}^{\tau,k}(r).$$

Therefore, we need only prove that $\tilde{r} \in \mathcal{B}$.

We prove by contradiction. If $\tilde{r} \notin \mathcal{B}$, there is a set $A \in \Omega$ and a constant $0 < C_0 < \frac{1}{2}$, such that $|A| > 0$ and

$$0 < C_0 < \tilde{r}_1(\mathbf{x}), \tilde{r}_2(\mathbf{x}) < 1 - C_0, \quad \text{for all } \mathbf{x} \in A.$$

We divide A into two sets $A = A_1 \cup A_2$ such that $A_1 \cap A_2 = \emptyset$ and $|A_1| = |A_2| = |A|/2$. Denote $r^t = (r_1^t, r_2^t)$ where $r_1^t = \tilde{r}_1 + t\chi_{A_1} - t\chi_{A_2}$ and $r_2^t = \tilde{r}_2 - t\chi_{A_1} + t\chi_{A_2}$ with χ_{A_1} and χ_{A_2} being the indicator functions of the domain A_1 and A_2 , respectively. When $0 < t < C_0$, we have $0 < r_1^t, r_2^t < 1$ and

$$r_1^t + r_2^t = \tilde{r}_1 + \tilde{r}_2 = 1, \quad \text{and} \quad \int_{\Omega} r_1^t \, d\mathbf{x} = \int_{\Omega} \tilde{r}_1 \, d\mathbf{x} = V_0.$$

This implies that $r^t \in \mathcal{H}$. Furthermore, direct computations give,

$$\begin{aligned} \frac{d^2}{dt^2} \tilde{J}^{\tau,k}(r) &= 2\gamma \frac{\sqrt{\pi}}{\sqrt{\tau}} \int_{\Omega} \frac{d}{dt} r_1^t G_{\tau} * \frac{d}{dt} r_2^t \, d\mathbf{x} \\ &= 2\gamma \frac{\sqrt{\pi}}{\sqrt{\tau}} \int_{\Omega} (\chi_{A_1} - \chi_{A_2}) G_{\tau} * (\chi_{A_2} - \chi_{A_1}) \, d\mathbf{x} \\ &= -2\gamma \frac{\sqrt{\pi}}{\sqrt{\tau}} \int_{\Omega} (\chi_{A_1} - \chi_{A_2}) G_{\tau} * (\chi_{A_1} - \chi_{A_2}) \, d\mathbf{x} \\ &= -2\gamma \frac{\sqrt{\pi}}{\sqrt{\tau}} \int_{\Omega} (G_{\tau/2} * (\chi_{A_1} - \chi_{A_2})) (G_{\tau/2} * (\chi_{A_1} - \chi_{A_2})) \, d\mathbf{x} \\ &\leq 0. \end{aligned}$$

The penultimate step comes from the fact that the heat kernel is a self-adjoint operator and forms a semigroup with various values of τ . From the above inequality, the functional is concave on the point \tilde{r} . Thus, \tilde{r} cannot be a minimizer of the functional. This contradicts the assumption. \square

Now, we show that (3.13) can be solved with a simple threshold dynamics method. Because $\tilde{J}^{\tau,k}(r)$ is quadratic in r and concave, we first linearize the energy $\tilde{J}^{\tau,k}(r)$ at r^k by

$$(3.16) \quad \tilde{J}^{\tau,k}(r) \approx \tilde{J}^{\tau,k}(r^k) + \mathcal{L}_{r^k}^{\tau,k}(r - r^k),$$

where

$$(3.17) \quad \begin{aligned} \mathcal{L}_{r^k}^{\tau,k}(r) &= \int_{\Omega} \left(\gamma \sqrt{\frac{\pi}{\tau}} r_1 G_{\tau} * r_2^k + \gamma \sqrt{\frac{\pi}{\tau}} r_2 G_{\tau} * r_1^k + r_2 \frac{\bar{\alpha}}{2} G_{\tau} * |\mathbf{u}^k|^2 \right) \, d\mathbf{x} \\ &= \int_{\Omega} (r_1 \phi_1 + r_2 \phi_2) \, d\mathbf{x}. \end{aligned}$$

Here $\phi_1 = \gamma \sqrt{\frac{\pi}{\tau}} G_{\tau} * r_2^k$ and $\phi_2 = \frac{\bar{\alpha}}{2} G_{\tau} * |\mathbf{u}^k|^2 + \gamma \sqrt{\frac{\pi}{\tau}} G_{\tau} * r_1^k$. Then (3.13) can be approximately reformulated into

$$(3.18) \quad \chi^{k+1} = \arg \min_{r \in \mathcal{H}} \mathcal{L}_{r^k}^{\tau,k}(r) = \arg \min_{r \in \mathcal{H}} \int_{\Omega} (r_1 \phi_1 + r_2 \phi_2) \, d\mathbf{x}.$$

The following lemma, in particular, (3.21) shows that (3.18) can be solved in a pointwise manner by

$$(3.19) \quad \begin{cases} \chi_1^{k+1}(\mathbf{x}) = 1 \text{ and } \chi_2^{k+1}(\mathbf{x}) = 0, & \text{if } \phi_1(\mathbf{x}) < \phi_2(\mathbf{x}) + \delta, \\ \chi_1^{k+1}(\mathbf{x}) = 0 \text{ and } \chi_2^{k+1}(\mathbf{x}) = 1, & \text{otherwise,} \end{cases}$$

where δ is chosen as a constant such that $\int_{\Omega} \chi_1^{k+1} \, d\mathbf{x} = V_0$.

Lemma 3.3. Let $\phi_1 = \gamma \sqrt{\frac{\pi}{\tau}} G_{\tau} * \chi_2^k$, $\phi_2 = \frac{\bar{\alpha}}{2} G_{\tau} * |\mathbf{u}^k|^2 + \gamma \sqrt{\frac{\pi}{\tau}} G_{\tau} * \chi_1^k$,

$$(3.20) \quad D_1^{k+1} = \{\mathbf{x} \in \Omega \mid \phi_1 - \phi_2 < \delta\}$$

for some δ such that $|D_1^{k+1}| = V_0$, and $D_2^{k+1} = \Omega \setminus D_1^{k+1}$. Then for $\chi^{k+1} = (\chi_1^{k+1}, \chi_2^{k+1})$ with $\chi_1^{k+1} = \chi_{D_1^{k+1}}$ and $\chi_2^{k+1} = 1 - \chi_1^{k+1}$, we have

$$\mathcal{L}_{\chi^k}^{\tau,k}(\chi^{k+1}) \leq \mathcal{L}_{\chi^k}^{\tau,k}(\chi^k)$$

for all $\tau > 0$.

Proof. Because $\mathcal{L}_{\chi^k}^{\tau,k}$ is a linear functional, we only need to prove that there holds

$$(3.21) \quad \mathcal{L}_{\chi^k}^{\tau,k}(\chi^{k+1}) \leq \mathcal{L}_{\chi^k}^{\tau,k}(\chi)$$

for all $\chi = (\chi_1, \chi_2) \in \mathcal{B}$.

For each $(\chi_1, \chi_2) \in \mathcal{B}$, we know $\chi_1 = \chi_{\hat{D}_1}$ and $\chi_2 = \chi_{\hat{D}_2}$ for some open sets \hat{D}_1, \hat{D}_2 in Ω , such that $\hat{D}_1 \cap \hat{D}_2 = \emptyset$, $\hat{D}_1 \cup \hat{D}_2 = \Omega$ and $|\hat{D}_1| = V_0$. Let $A_1 = \hat{D}_1 \setminus D_1^{k+1} = D_2^{k+1} \setminus \hat{D}_2$ and $A_2 = \hat{D}_2 \setminus D_2^{k+1} = D_1^{k+1} \setminus \hat{D}_1$. We must have $|A_1| = |A_2|$ due to the volume conservation property. Because $A_1 \subset D_2^{k+1}$, we have

$$\phi_1(\mathbf{x}) - \phi_2(\mathbf{x}) \geq \delta, \quad \chi_1^{k+1}(\mathbf{x}) - \chi_1(\mathbf{x}) = -1, \quad \forall \mathbf{x} \in A_1.$$

Similarly, because $A_2 \subset D_1^{k+1}$, we have

$$\phi_1(\mathbf{x}) - \phi_2(\mathbf{x}) < \delta, \quad \chi_1^{k+1}(\mathbf{x}) - \chi_1(\mathbf{x}) = 1, \quad \forall \mathbf{x} \in A_2.$$

Therefore, using $\chi_1^{k+1} - \chi_1 + \chi_2^{k+1} - \chi_2 = 0$, we have

$$\begin{aligned} \mathcal{L}_{\chi^k}^{\tau,k}(\chi^{k+1}) - \mathcal{L}_{\chi^k}^{\tau,k}(\chi) &= \gamma \sqrt{\frac{\pi}{\tau}} \int_{\Omega} (\chi_1^{k+1} - \chi_1) \phi_1 + (\chi_2^{k+1} - \chi_2) \phi_2 \, d\mathbf{x} \\ &= \gamma \sqrt{\frac{\pi}{\tau}} \int_{\Omega} (\chi_1^{k+1} - \chi_1) (\phi_1 - \phi_2) \, d\mathbf{x} \\ &= \gamma \sqrt{\frac{\pi}{\tau}} \int_{\Omega} (\chi_{A_2} (\phi_1 - \phi_2) - \chi_{A_1} (\phi_1 - \phi_2)) \, d\mathbf{x} \\ &\leq \gamma \sqrt{\frac{\pi}{\tau}} \int_{\Omega} (\chi_{A_2} \delta - \chi_{A_1} \delta) \, d\mathbf{x} = \gamma \sqrt{\frac{\pi}{\tau}} \delta (|A_2| - |A_1|) = 0. \end{aligned}$$

□

To determine the value of δ , one can treat $\int_{\Omega} \chi_1^{k+1} \, d\mathbf{x} - V_0$ as a function of δ and use an iteration method (e.g., bisection method or Newton's method) to find the root of $\int_{\Omega} \chi_1^{k+1} \, d\mathbf{x} - V_0 = 0$. For the uniform discretization of Ω , a more efficient method is the quick-sort technique proposed in [69]. Assume we have a uniform discretization of Ω with grid size h , we can approximate $\int_{\Omega} \chi_1^{k+1} \, d\mathbf{x}$ by Mh^2 , we then sort the values of $\phi_1 - \phi_2$ in an ascending order and simply set $\chi_1^{k+1} = 1$ on the first M points and $\chi_2^{k+1} = 1$ on the other points.

Remark 3.2. In many implementations, one may solve Stokes equation on nonuniform grid points. To preserve the volume for the discretization on nonuniform grids, although the volume cannot be simply approximated by the number of grid points times the size of each cell, a similar technique can be applied. One can still sort the values of $\phi_1 - \phi_2$ in ascending order, save the index into \mathcal{S} , calculate the integrating weight at each grid point into \mathcal{V} , and set $V = 0$ and $i = 0$. Then, δ can be simply found by:

$$\text{while } V < V_0; \quad i \leftarrow i + 1; \quad V = V + \mathcal{V}(\mathcal{S}(i)); \quad \text{end}; \quad \delta = \phi_1(\mathcal{S}(i + 1)) - \phi_2(\mathcal{S}(i + 1)).$$

Now, we are led to a threshold dynamics algorithm for topology optimization problem (3.6) for fluids in Stokes flow in the following.

Algorithm 1. Discretize Ω uniformly into a grid \mathcal{T}_h with grid size h and set $M = V_0/h^d$.

Step 1. Input: Set $\tau > 0$, $\bar{\alpha} > 0$, $k = 0$, a tolerance parameter $tol > 0$ and give the initial guess $\chi^0 \in \mathcal{B}$.

Step 2. Iterative solution:

1. **Update \mathbf{u} .** Solve the Brinkman flow equations

$$\begin{cases} \nabla \cdot \mathbf{u} = 0, & \text{in } \Omega \\ \nabla p - \nabla \cdot (\mu \nabla \mathbf{u}) + \alpha(\chi^k) \mathbf{u} = \mathbf{f}, & \text{in } \Omega \\ \mathbf{u}|_{\partial\Omega} = \mathbf{u}_D \end{cases}$$

by mixed finite-element method to get \mathbf{u}^k , where $\alpha(\chi^k) = \bar{\alpha}G_\tau * \chi_2^k$.

2. Update χ . Evaluate

$$\begin{cases} \phi_1 = \gamma\sqrt{\frac{\pi}{\tau}}G_\tau * \chi_2^k, \\ \phi_2 = \frac{\bar{\alpha}}{2}G_\tau * |\mathbf{u}|^2 + \gamma\sqrt{\frac{\pi}{\tau}}G_\tau * \chi_1^k. \end{cases}$$

Sort the values of $\phi_1 - \phi_2$ in an ascending order, and set $\chi_1^{k+1} = 1$ on the first M points and $\chi_2^{k+1} = 1$ on the other points.

3. Compute $e_\chi^k = \|\chi_1^{k+1} - \chi_1^k\|_2$. If $e_\chi^k \leq \text{tol}$, stop the iteration and go to the output step. Otherwise, let $k + 1 \rightarrow k$ and continue the iteration.

Step 3. Output: A function $\chi \in \mathcal{B}$ that approximately solves (3.6).

Remark 3.3. We note that in the original MBO method, on one hand, the algorithm can be easily stuck when τ is very small because, in the discretized space, τ is so small that no point can switch from one phase to another (*i.e.*, χ_1 changes from 0 to 1 or 1 to 0) at one iteration step. On the other hand, with a large τ , the interface can easily move but creates large error. Hence, we apply the adaptive in time technique [69] in numerical experiments by modifying Algorithm 1 into an adaptive algorithm by adjusting τ during the iterations. Indeed, we set a threshold value τ_t and a given tolerance e_t , if $e_\chi^k \leq e_t$, let $\tau_{\text{new}} = \eta\tau$ with $\eta \in (0, 1)$ and update $\tau := \tau_{\text{new}}$ in the next iteration unless $\tau \leq \tau_t$. Otherwise, τ will not be updated, and the iteration will continue with the same τ . We use this adaptive strategy for the choice of τ in the numerical experiments.

Remark 3.4. As for the efficiency, because such approximation of the regularization term using the concave functional, we find the minimizer of the linear approximation which is the optimal choice to minimize the linearized functional. Moreover, the minimizer can give a smaller value of the energy because the graph of a concave functional is always below its linear approximation. This accelerates the minimization of the energy in the method.

4. STABILITY ANALYSIS

In this section, we prove the unconditional stability property of the proposed algorithm. Specifically, for the series of minimizers

$$\mathbf{u}^0, \chi^1, \mathbf{u}^1, \chi^2, \dots, \mathbf{u}^k, \chi^{k+1}, \dots,$$

computed by Algorithm 1, we prove

$$J^\tau(\chi^{k+1}, \mathbf{u}^{k+1}) \leq J^\tau(\chi^k, \mathbf{u}^k)$$

for all $\tau > 0$.

We first introduce Lemma 4.1 which leads us to $J^\tau(\chi^{k+1}, \mathbf{u}^k) \leq J^\tau(\chi^k, \mathbf{u}^k)$ for all $\tau > 0$.

Lemma 4.1. *For a fixed \mathbf{u}^k , let χ^{k+1} be the $k + 1$ -th iteration derived from Algorithm 1, we have*

$$J^\tau(\chi^{k+1}, \mathbf{u}^k) \leq J^\tau(\chi^k, \mathbf{u}^k)$$

for all $\tau > 0$.

Proof. From the linearization of $\tilde{J}^{\tau,k}(\chi^k)$ in (3.16), we have

$$\begin{aligned} J^\tau(\chi^k, \mathbf{u}^k) &= \mathcal{L}_{\chi^k}^{\tau,k}(\chi^k) - \gamma\sqrt{\frac{\pi}{\tau}} \int_{\Omega} \chi_1^k G_\tau * \chi_2^k \, dx + \int_{\Omega} \frac{\mu}{2} |D\mathbf{u}^k|^2 - \mathbf{u}^k \cdot \mathbf{f} \, dx, \\ J^\tau(\chi^{k+1}, \mathbf{u}^k) &= \mathcal{L}_{\chi^k}^{\tau,k}(\chi^{k+1}) - \gamma\sqrt{\frac{\pi}{\tau}} \int_{\Omega} (\chi_1^{k+1} G_\tau * \chi_2^k + \chi_2^{k+1} G_\tau * \chi_1^k - \chi_1^{k+1} G_\tau * \chi_2^{k+1}) \, dx \\ &\quad + \int_{\Omega} \frac{\mu}{2} |D\mathbf{u}^k|^2 - \mathbf{u}^k \cdot \mathbf{f} \, dx. \end{aligned}$$

Then, we calculate

$$\begin{aligned}
J^\tau(\chi^{k+1}, \mathbf{u}^k) - J^\tau(\chi^k, \mathbf{u}^k) &= \mathcal{L}_{\chi^k}^{\tau,k}(\chi^{k+1}) - \mathcal{L}_{\chi^k}^{\tau,k}(\chi^k) + \gamma \sqrt{\frac{\pi}{\tau}} \int_{\Omega} (\chi_1^{k+1} - \chi_1^k) G_\tau * (\chi_2^{k+1} - \chi_2^k) \, d\mathbf{x} \\
&= \mathcal{L}_{\chi^k}^{\tau,k}(\chi^{k+1}) - \mathcal{L}_{\chi^k}^{\tau,k}(\chi^k) - \gamma \sqrt{\frac{\pi}{\tau}} \int_{\Omega} (\chi_1^{k+1} - \chi_1^k) G_\tau * (\chi_1^{k+1} - \chi_1^k) \, d\mathbf{x} \\
&= \mathcal{L}_{\chi^k}^{\tau,k}(\chi^{k+1}) - \mathcal{L}_{\chi^k}^{\tau,k}(\chi^k) - \gamma \sqrt{\frac{\pi}{\tau}} \int_{\Omega} (G_{\tau/2} * (\chi_1^{k+1} - \chi_1^k))^2 \, d\mathbf{x} \\
&\leq \mathcal{L}_{\chi^k}^{\tau,k}(\chi^{k+1}) - \mathcal{L}_{\chi^k}^{\tau,k}(\chi^k).
\end{aligned}$$

Because we have $\mathcal{L}_{\chi^k}^{\tau,k}(\chi^{k+1}) - \mathcal{L}_{\chi^k}^{\tau,k}(\chi^k) \leq 0$ from Lemma 3.3, we are led to

$$J^\tau(\chi^{k+1}, \mathbf{u}^k) - J^\tau(\chi^k, \mathbf{u}^k) \leq 0$$

for all $\tau > 0$. □

We are now led to the following theorem which proves the total energy decaying property

Theorem 4.2. *For the series of minimizers*

$$\mathbf{u}^0, \chi^1, \mathbf{u}^1, \chi^2, \dots, \mathbf{u}^k, \chi^{k+1}, \dots,$$

calculated with Algorithm 1, we have

$$(4.1) \quad J^\tau(\chi^{k+1}, \mathbf{u}^{k+1}) \leq J^\tau(\chi^k, \mathbf{u}^k)$$

for all $\tau > 0$.

Proof. For all $\tau > 0$, from (3.7), we have

$$J^\tau(\chi^{k+1}, \mathbf{u}^{k+1}) \leq J^\tau(\chi^{k+1}, \mathbf{u}^k).$$

From Lemma 4.1, we have

$$J^\tau(\chi^{k+1}, \mathbf{u}^k) \leq J^\tau(\chi^k, \mathbf{u}^k).$$

Thus, combining the above together gives the stability estimate (4.1). □

Remark 4.1. We remark here that, as we proved, the energy is decaying for any given τ . If τ changes from τ_1 to τ_2 at the k^{th} iteration with $\tau_1 > \tau_2$ in our adaptive in time strategy, for example, χ^k is generated by τ_1 and χ^{k+1} is generated by τ_2 . The energy is decaying in the sense that $J^{\tau_2}(\chi^{k+1}, \mathbf{u}^{k+1}) \leq J^{\tau_2}(\chi^k, \mathbf{u}^k)$ where the energy J at two iterations χ^k and χ^{k+1} are approximated by the same τ_2 .

5. NUMERICAL IMPLEMENTATION

In this section, we illustrate the implementation of Algorithm 1, with a focus on Step 2. The Brinkman equations (3.3a-3.3c) are solved with the mixed finite-element method, and the Taylor-Hood finite-element space is used for discretization, which satisfies the discrete inf-sup condition [28].

Let \mathcal{T}_h be a uniform triangulation of the domain Ω , and \mathcal{N}_h is the set of all vertices of \mathcal{T}_h . For a given $\bar{\chi}_h = (\bar{\chi}_1^h, \bar{\chi}_2^h) \in \mathcal{B}_h$ where \mathcal{B}_h is the discrete version of \mathcal{B} defined on \mathcal{N}_h . For the uniform regular triangulation of the domain, all values are evaluated on uniform quad grid points. Thus, we can use FFT for efficient evaluation of the discretized convolutions.

We introduce the Taylor-Hood finite-element space

$$\mathbf{V}_h := \{\mathbf{v} \in H^1(\Omega, \mathbb{R}^d) \mid \mathbf{v}|_K \in [P_2(K)]^d, K \in \mathcal{T}_h\},$$

$$Q_h := \{q \in L^2(\Omega, \mathbb{R}) \mid \int_{\Omega} q \, d\mathbf{x} = 0, q|_K \in P_1(K), K \in \mathcal{T}_h\}.$$

Let $\mathbf{V}_h^D := \{\mathbf{v} \in \mathbf{V}_h \mid \mathbf{v}|_{\partial\Omega} = \mathbf{u}_D^h\}$, where \mathbf{u}_D^h is a suitable approximation of the Dirichlet boundary condition \mathbf{u}_D on the boundary edges/faces of \mathcal{T}_h . For the solution of (3.3a-3.3c), find $(\mathbf{u}_h, p_h) \in \mathbf{V}_h^D \times Q_h$ such that

$$\begin{aligned}
-(p_h, \nabla \cdot \mathbf{v}_h) + (\mu \nabla \mathbf{u}_h, \nabla \mathbf{v}_h) + (\alpha(\bar{\chi}_h) \mathbf{u}_h, \mathbf{v}_h) &= (\mathbf{f}, \mathbf{v}_h), \quad \forall \mathbf{v}_h \in \mathbf{V}_h^0, \\
(\nabla \cdot \mathbf{u}_h, q_h) &= 0, \quad \forall q_h \in Q_h.
\end{aligned}$$

The above bilinear form can be easily extended to the Brinkman equations both with Dirichlet boundary Γ_D and Neumann boundary Γ_N , where $\Gamma_D \cap \Gamma_N = \emptyset$, $\Gamma_D \cup \Gamma_N = \partial\Omega$, and $(\mu\nabla\mathbf{u} - p\mathbf{I}) \cdot \mathbf{n}|_{\Gamma_N} = \mathbf{g}$.

When \mathbf{u}_h is obtained, we proceed to use the FFT to evaluate (ϕ_1^h, ϕ_2^h) on each node of \mathcal{N}_h as follows:

$$\begin{cases} \phi_1^h = \gamma\sqrt{\frac{\pi}{\tau}}G_\tau * \bar{\chi}_2^h, \\ \phi_2^h = \frac{\bar{\alpha}}{2}G_\tau * |\mathbf{u}_h|^2 + \gamma\sqrt{\frac{\pi}{\tau}}G_\tau * \bar{\chi}_1^h. \end{cases}$$

Following Algorithm 1, we can now use (ϕ_1^h, ϕ_2^h) to update the indicator function χ_h by the approach stated in Algorithm 1.

6. NUMERICAL EXPERIMENTS

In this section, we perform extensive numerical testing to demonstrate the efficiency of Algorithm 1 with an adaptive strategy for the choice of τ . We choose $\eta = 0.5$ in the update of τ . If no confusion is possible, we still denote by τ as its initialization in the following.

6.1. Two dimensional results. We firstly test the proposed algorithm for the two dimensional problems. For most of examples in this subsection, we assume that the Dirichlet boundary condition with a parabolic profile and the magnitude of the velocity is set as $|\mathbf{u}_D| = \bar{y}(1 - (2t/l)^2)$ with $t \in [-l/2, l/2]$, where l is the length of the section of the boundary at which the inflow/outflow velocity is imposed. The direction of the inflow/outflow velocity is illustrated in the following examples.

Example 6.1. The first example shown in Figure 6.1 is the optimal design of a diffuser that was tested for topology optimization for fluids using MMA in [12]. Here, we apply Algorithm 1 to obtain the optimal design of the diffuser. Let $\bar{y} = 1$ and 3 for the inflow and outflow velocities, respectively. We first set the fluid region fraction as $\beta = 0.5$ and test the problem on a 128×128 grid.

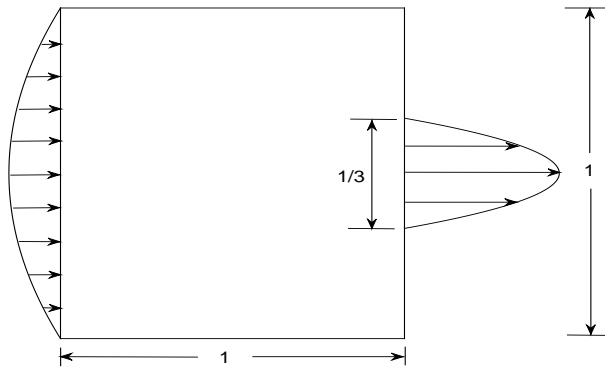


FIGURE 6.1. (Example 6.1) Design domain for the diffuser example.

We first perform the simulations with $\bar{\alpha} = 2.5 \times 10^4$, $\tau = 0.01$, $\gamma = 0.1$ and with two types of initial distribution of χ_1 , as shown in Figure 6.2; that is, the initial fluid region is restricted in the middle of the domain in the left graph of Figure 6.2 (Case 1), and the initial fluid region satisfies a random distribution in the right graph of Figure 6.2 (Case 2). In both cases, from the experiments we did so far (i.e., with different random initial conditions in Case 2), we always arrive at the same optimal design result shown in the left graph of Figure 6.3, which also shows the quiver plot of the approximate velocity in the fluid region. The optimal design result seems similar to the result obtained by MMA in [12]. The energy decaying property can be observed in the right graph of Figure 6.3 which shows the energy curves for the above two cases of the initial distribution of χ_1 . The iteration converges in about 25 steps in both cases.

Next, we test the case (initial fluid region of Case 1) for various parameters. We first fix $\bar{\alpha} = 2.5 \times 10^4$, $\tau = 0.01$ and vary $\gamma = 0.01, 0.005, 0.001$. We then test the cases for fixed $\gamma = 0.001$ and various choices of $\tau = 0.05, 0.01, 0.001$. The optimal design of the diffuser is similar to the result in the left graph of Figure 6.3.

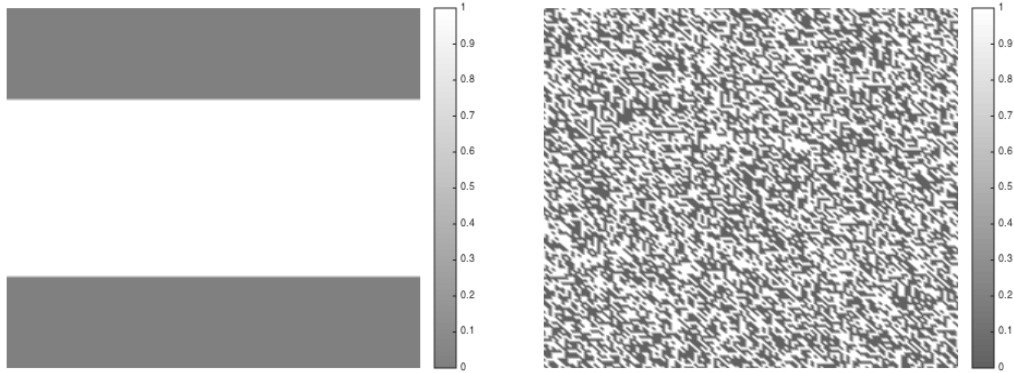


FIGURE 6.2. (Example 6.1) Left (Case 1): Initial distribution of χ_1 . Right (Case 2): Initial distribution of χ_1 .

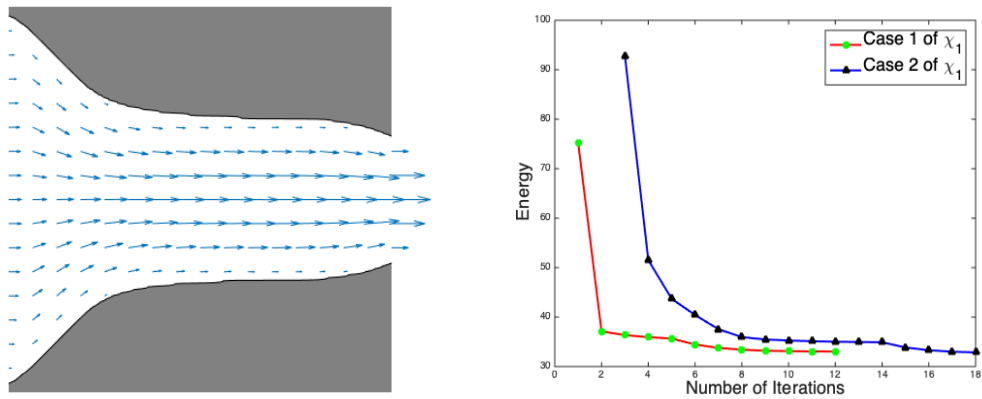


FIGURE 6.3. (Example 6.1) Left: Optimal diffuser for the case $\bar{\alpha} = 2.5 \times 10^4$ and the approximate velocity in the fluid region. Right: Plot of energy curves for two cases of distribution of χ_1 . In this case, the parameters are set as $\bar{\alpha} = 2.5 \times 10^4$, $\tau = 0.01$, $\gamma = 0.1$.

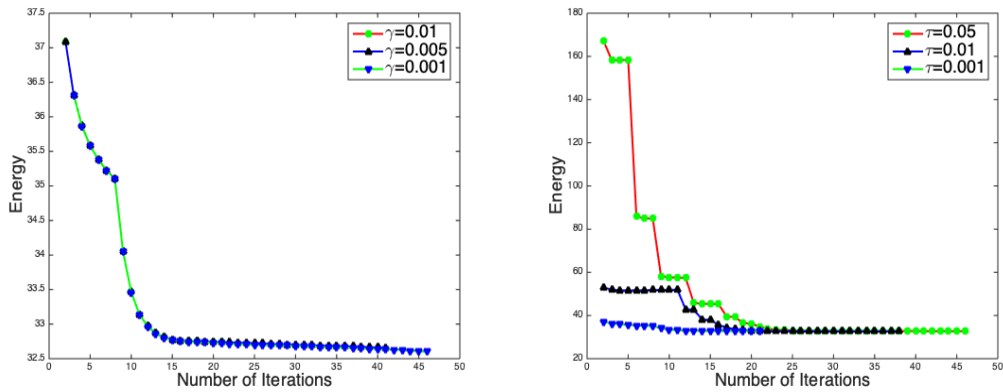


FIGURE 6.4. (Example 6.1) Plot of energy curves for case 1 of distribution of χ_1 with $\bar{\alpha} = 2.5 \times 10^4$. Left: For fixed $\tau = 0.01$, energy curves for the cases of $\gamma = 0.01, 0.005, 0.001$. Right: For fixed $\gamma = 0.01$, energy curves for the cases of $\tau = 0.05, 0.01, 0.001$.

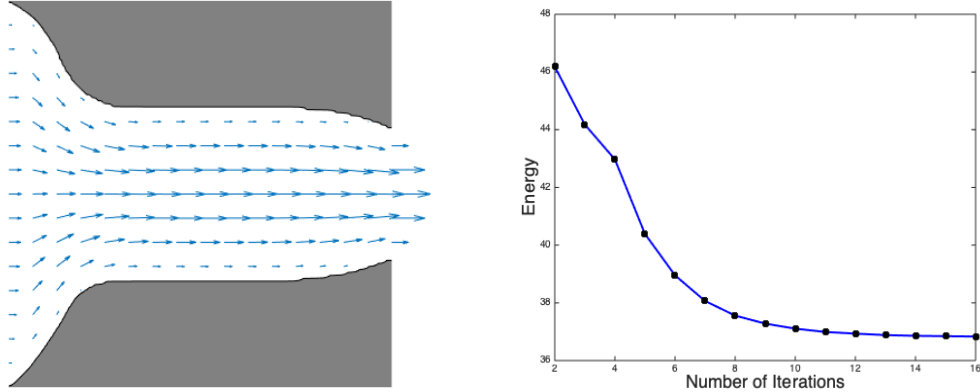


FIGURE 6.5. (Example 6.1) Left: Associated optimal diffuser and approximate velocity in the fluid region. Right: Plot of energy curve for Case 1 of distribution of χ_1 . In this case, the parameters are set as $\bar{\alpha} = 2.5 \times 10^5$, $\tau = 0.001$, $\gamma = 0.01$.

Figure 6.4 shows the energy decaying property for each of these cases. In all cases, the iteration converges in fewer than 25 steps.

In the next example, we increase $\bar{\alpha} = 2.5 \times 10^5$. Again, we use the initial fluid region of Case 1 with $\tau = 0.001, \gamma = 0.01$. The optimal design of the diffuser and the approximate velocity in the fluid region are shown in the left graph of Figure 6.5. It seems that the fluid region at the left boundary reaches top and bottom boundaries in this case. The energy decaying property is also observed in Figure 6.5. The iteration converges even more quickly at about 10 steps.

In order to further show the robustness of our algorithm, in the following we fix τ, γ and compare the numerical results of our algorithm with different choices of the parameter β . Here β is related to the parameter M in Algorithm 1. We test with the initial fluid region of Case 1 in Figure 6.2. The optimal design of the diffuser (see Figure 6.6) is obtained respectively for different choices of β , and we can see from Table 1 that our algorithm always stably converges in fewer than 30 steps.

β	Number of iterations
1/3	27
2/5	29
2/3	27
3/4	25

TABLE 1. The number of iterations of our algorithm for Example 6.1 with $\bar{\alpha} = 2.5 \times 10^4$ by different choices of β and fixed $\tau = 0.01$ and $\gamma = 0.001$.

We also test the problem with the same inflow Dirichlet boundary condition as above, but we replace the outflow Dirichlet boundary condition with a homogeneous Neumann boundary. A similar optimal design of diffuser is then obtained as above for the cases of $\bar{\alpha} = 2.5 \times 10^4$ and $\bar{\alpha} = 2.5 \times 10^5$.

Example 6.2. In this example, we test the double pipes problem shown in Figure 6.7. The inflow and outflow Dirichlet boundaries are located with centers $[0, 1/4], [0, 3/4], [1, 1/4], [1, 3/4]$, as shown in Figure 6.7. Let $\bar{g} = 1$ for the inflow and outflow velocities, respectively, and let the fluid region fraction be $\beta = 1/3$. We test the problem with $\bar{\alpha} = 2.5 \times 10^4$ on a 128×256 grid for $d = 0.5$ and on a 192×128 grid for $d = 1.5$.

For the case $d = 0.5$, we choose a random initial distribution χ_1 , as shown in the left graph of Figure 6.8. We remark that γ can also be set to zero in Algorithm 1. For fixed $\tau = 0.001$, we test $\gamma = 0.01, 0.001, 0$. The optimal design result is nearly the same for the three choices of γ , as shown in the middle graph of Figure 6.8, and the energy decaying property is observed from the energy curves in the right graph of Figure 6.8.

For the case $d = 1.5$, we choose an initial distribution χ_1 with the fluid region located in the middle of the domain as Case 1 of Example 6.1. We set $\tau = 0.01$ and $\gamma = 0.0001$. The optimal design result and the approximate velocity are shown in the left graph of Figure 6.9, and the energy decaying property is also

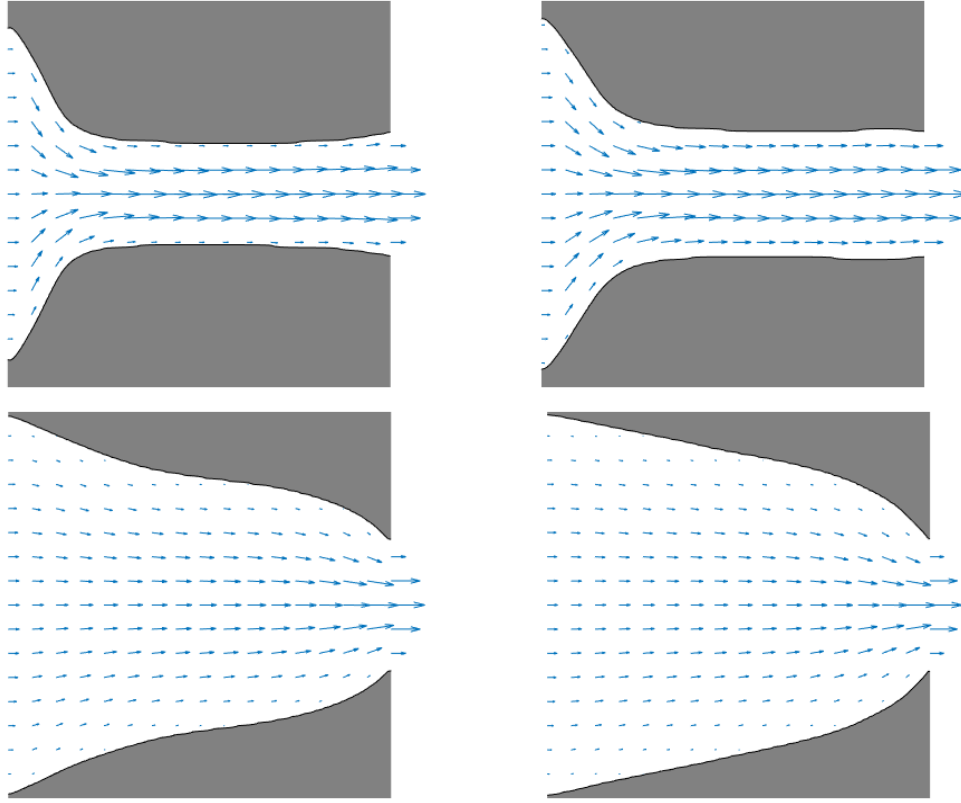


FIGURE 6.6. (Example 6.1) Associated optimal diffuser and approximate velocity in the fluid region based on different choices β . Top-left: $\beta = 1/3$; Top-right: $\beta = 2/5$; Bottom-left: $\beta = 2/3$; Bottom-right: $\beta = 3/4$. In this case, we fix the parameters as $\bar{\alpha} = 2.5 \times 10^4$, $\tau = 0.01$, $\gamma = 0.001$.

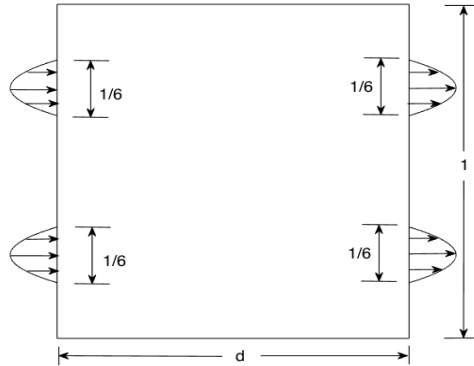


FIGURE 6.7. (Example 6.2) Design domain for the double pipes example.

observed from the energy curve in the right graph of Figure 6.9. For the large jump in this energy curve at the iteration steps 9 and 10, we observe that this is due to the fact that there is a large topology change of the fluid and solid regions at these two steps. Compared with the computational cost used by MMA in [12], we find that our algorithm converges more quickly to the optimal result.

Example 6.3. We consider another example studied in [12] that includes a body fluid force term imposed in the local circular region with center $[1/2, 1/3]$ and radius $r = 1/12$. We show the design domain in Figure

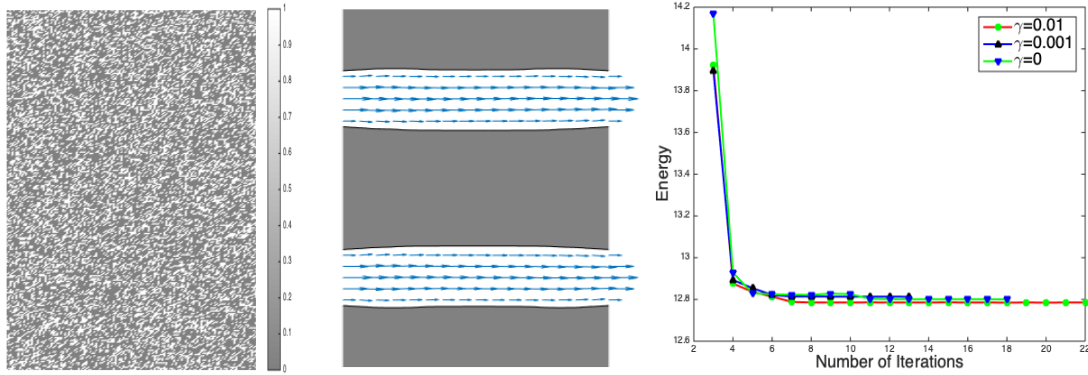


FIGURE 6.8. (Example 6.2) For the case $d = 0.5$. Left: Initial distribution of χ_1 . Middle: Optimal double pipes and approximate velocity in the fluid region. Right: For fixed $\tau = 0.001$, energy curves for the cases of $\gamma = 0.01, 0.001, 0$.

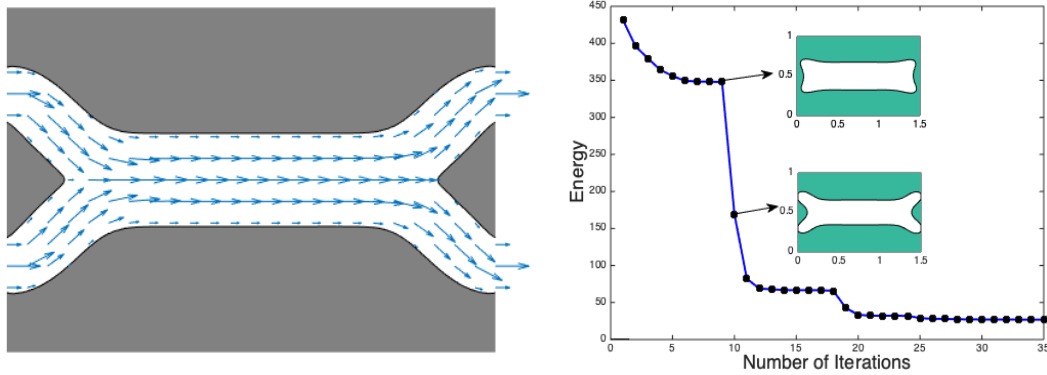


FIGURE 6.9. (Example 6.2) For the case $d = 1.5$, the parameters are set as $\tau = 0.01$ and $\gamma = 0.0001$. Left: Optimal double pipes and approximate velocity in fluid region. Right: Energy curve.

6.10. The inflow and outflow Dirichlet boundaries are located with centers $[0, 2/3]$ and $[1, 2/3]$ respectively. Let $\bar{g} = 1$ for the inflow and outflow velocities, and let the fluid region fraction be $\beta = 1/4$. We test the problem with various choices of body fluid force on a 128×128 grid, and we always choose $\bar{\alpha} = 2.5 \times 10^4$, $\tau = 0.01$, $\gamma = 0.0001$ in this example.

We test the cases for three different force terms $\mathbf{f} = [-1125, 0]$, $[562.5, 0]$, $[1687.5, 0]$. We choose the initial distribution χ_1 with the fluid region located in a circular region with center $[1/2, 1/2]$ and radius $1/\sqrt{3\pi}$. The optimal results and energy curves are plotted in Figures 6.11 to 6.13 for various values for force \mathbf{f} , and the new algorithm also converges more quickly to the optimal results than the MMA shown in [12]. One can observe that for $\mathbf{f} = [-1125, 0]$ the fluid flow is in a clockwise direction near the center roundabout (left graphs in Figure 6.11), while for $\mathbf{f} = [1687.5, 0]$ it is in a counterclockwise direction (left graph of Figure 6.13).

An interesting phenomenon observed in this example was the appearance of a tiny local solid at the center of the roundabout for the two cases of $\mathbf{f} = [-1125, 0]$, $[1687.5, 0]$, and the tiny local solid is clearer when the grid is finer (cf. Figure 6.14).

Example 6.4. Finally, we consider optimal design for a three-terminal device shown in Figure 6.15. The inflow and outflow Dirichlet boundaries are located with centers $[0, 0.3]$ and $[1, 0.7]$, and the homogeneous Neumann boundary is located on the left boundary with center $[0, 1.1]$. Let $\bar{g} = 0.5$ for the inflow velocity and the fluid region fraction be $\beta = 0.3$. We choose $\bar{\alpha} = 2.5 \times 10^4$, $\tau = 0.01$, $\gamma = 0.0001$ in this example and test the problem on a grid 80×112 .

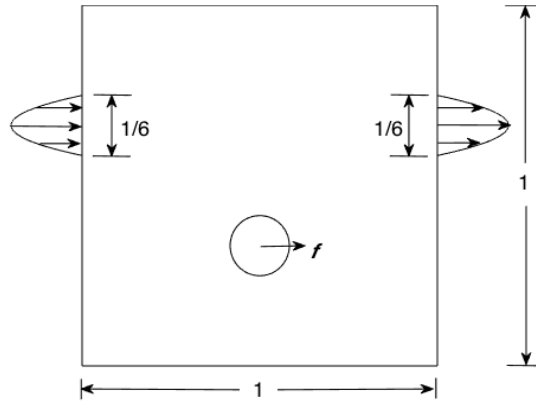


FIGURE 6.10. (Example 6.3) Design domain for the example with a force term.

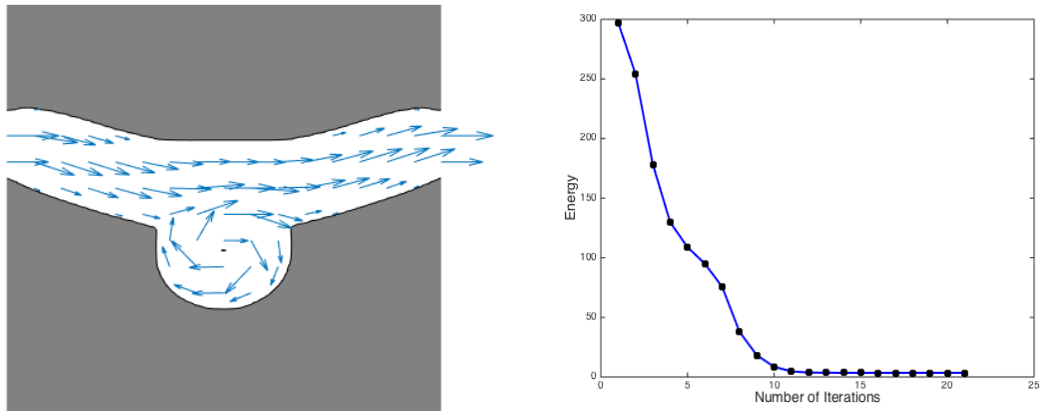


FIGURE 6.11. (Example 6.3) For the example with a force term $f = [-1125, 0]$ on a grid 128×128 . Left: Optimal design result and approximate velocity in the fluid region. Right: Energy curve.

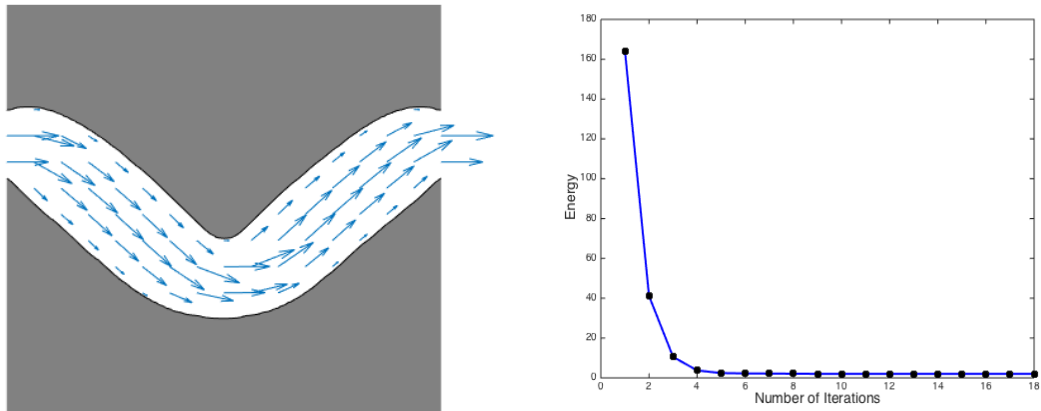


FIGURE 6.12. (Example 6.3) For the example with a force term $[562.5, 0]$ on a grid 128×128 . Left: Optimal design result and approximate velocity in the fluid region. Right: Energy curve.

We choose the initial distribution χ_1 , with the fluid region located in double parallel pipes $[0, 1] \times [13/60, 23/60] \cup [0, 1] \times [37/60, 47/60]$. The optimal result was obtained after 29 iterations. The optimal design result and the approximate velocity are shown in the left graph of Figure 6.16. The energy decaying property is also observed from the energy curve in the right graph of Figure 6.16.

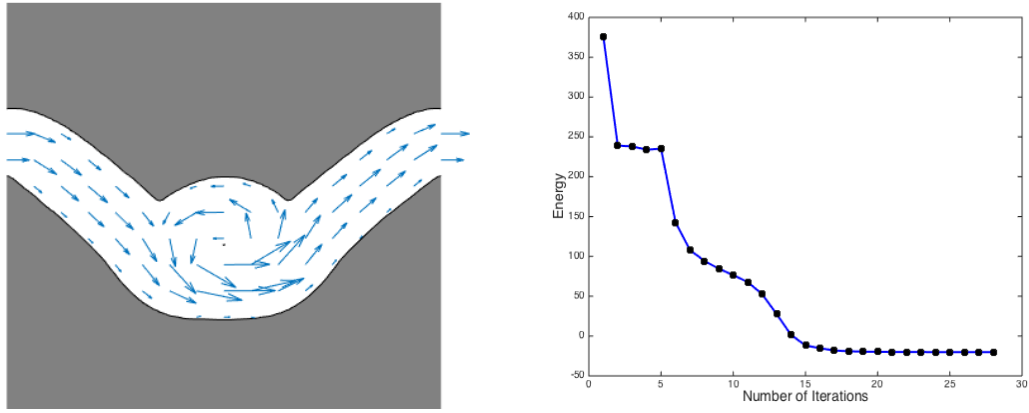


FIGURE 6.13. (Example 6.3) For the example with a force term $[1687.5, 0]$ on a grid 128×128 . Left: Optimal design result and approximate velocity in the fluid region. Right: Energy curve.

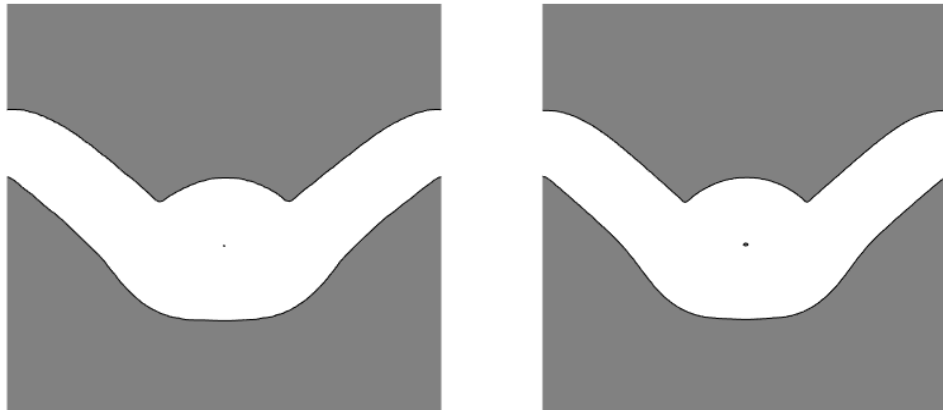


FIGURE 6.14. (Example 6.3) Optimal design results for for example with force term $f = [1687.5, 0]$. Left: Optimal design result on a coarse grid 128×128 . Right: Optimal design result on a fine grid 256×256 .

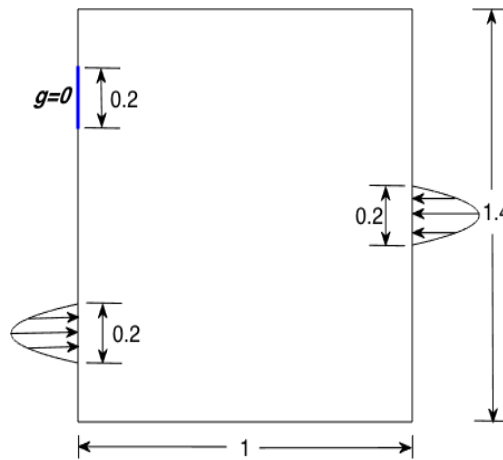


FIGURE 6.15. (Example 6.4) Design domain for the example with a force term.

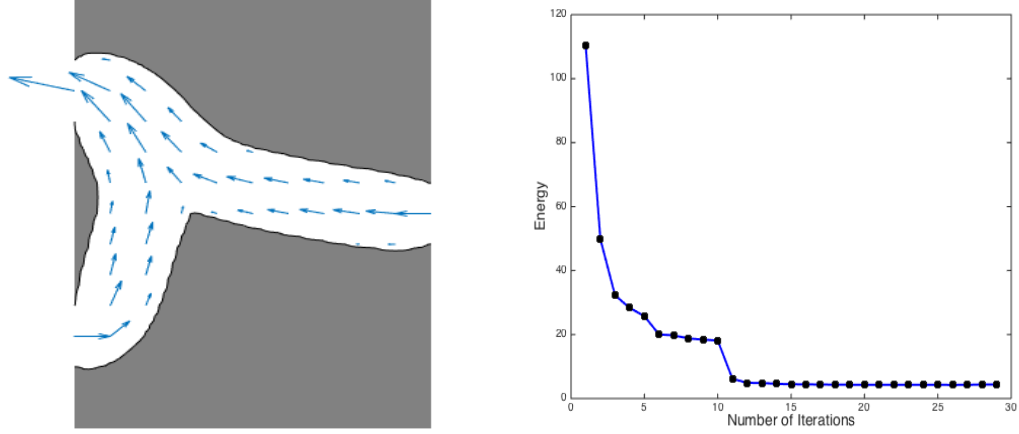


FIGURE 6.16. (Example 6.4) Left: Optimal design result for example of three-terminal device and approximate velocity in the fluid region. Right: Energy curve.

6.2. Three dimensional results. We now present the numerical examples in three dimensions. For the Dirichlet boundary condition in the following examples, we always assume that the magnitude of the velocity is set as

$$|\mathbf{u}_D| = \bar{g} \left(1 - \frac{(y - a)^2 + (z - b)^2}{l^2} \right),$$

where \bar{g} is the prescribed velocity at the center of the flow profile at which the inflow/outflow velocity is imposed, l is the radius of the flow profile, (y, z) are Cartesian coordinates on a x -plane, and (a, b) are the center of a circle on a x -plane.

Example 6.5. The design domain of this example is shown in Figure 6.17. For the inflow, we let $\bar{g} = 1$, $l = \frac{1}{2}$, and $(a, b) = (\frac{1}{2}, \frac{1}{2})$ on $x = 0$ plane. For the objective of mass conservation, we let $\bar{g} = 9$, $l = \frac{1}{6}$, and $(a, b) = (\frac{1}{2}, \frac{1}{2})$ on $x = 1$ plane. We set the fluid region fraction is $\beta = 0.35$. This example was already tested by the level set method in [14]. Here we apply our new Algorithm 1 to obtain the optimal diffuser. Throughout this example, we choose the initial distribution χ_1 with fluid domain in a region of $\{(x, y, z) : x \in (0, 1), y \in (0, 1), z \in (\frac{7}{20}, \frac{7}{10})\}$.

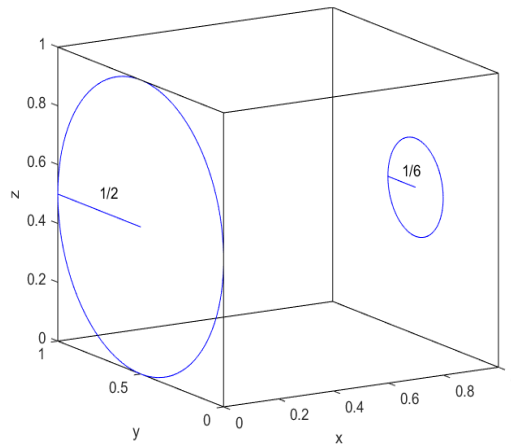


FIGURE 6.17. (Example 6.5) Design domain.

Firstly, we test the case with $\bar{\alpha} = 2.5 \times 10^4$, $\tau = 0.05$, and $\gamma = 0.01$ on $32 \times 32 \times 32$ and $64 \times 64 \times 64$ grids. In the following, the interface between solid and fluid regions for the optimal design is shown, and the fluid

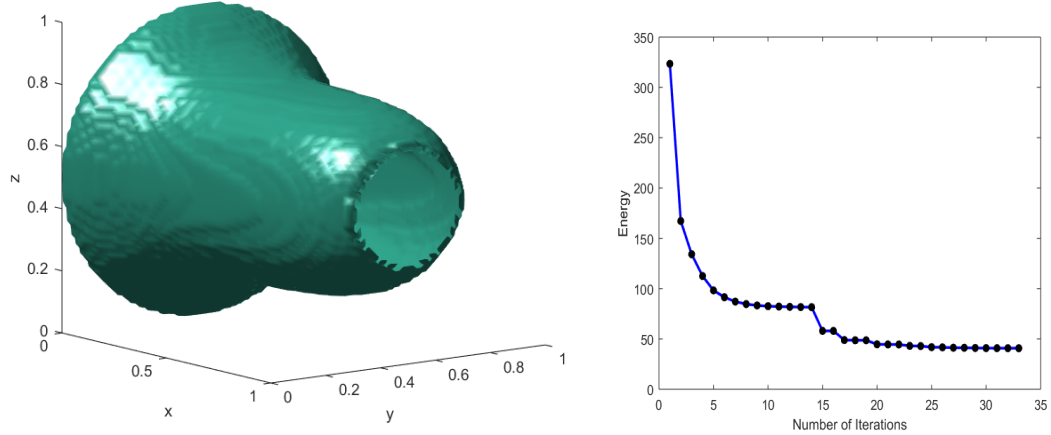


FIGURE 6.18. (Example 6.5) Left: Optimal design result on a $32 \times 32 \times 32$ grid. Right: Energy curve. In this case the parameters are set as $\bar{\alpha} = 2.5 \times 10^4$, $\tau = 0.05$, $\gamma = 0.01$.

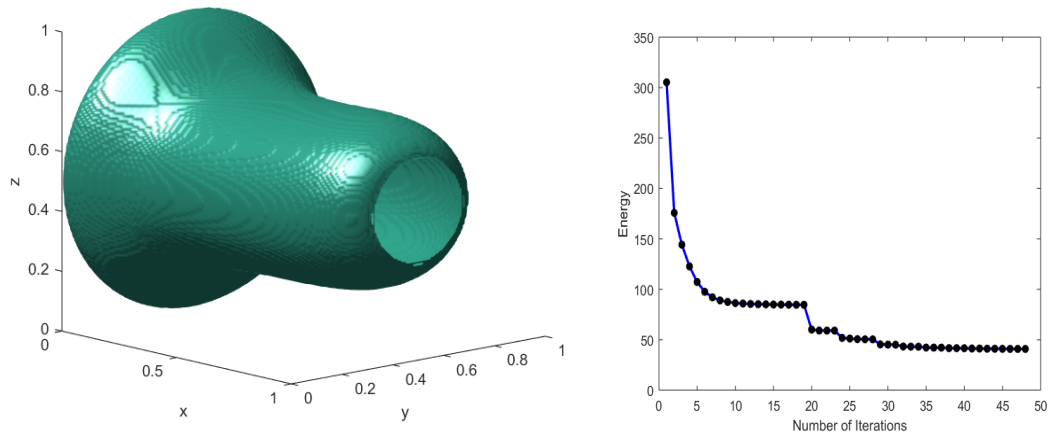


FIGURE 6.19. (Example 6.5) Left: Optimal design result on a $64 \times 64 \times 64$ grid. Right: Energy curve. In this case the parameters are set as $\bar{\alpha} = 2.5 \times 10^4$, $\tau = 0.05$, $\gamma = 0.01$.

region locates in the interior of subdomain surrounded by the interface. The optimal diffusers are presented in the left graphs of Figure 6.18 and Figure 6.19 and the energy decaying property can be observed in the right graphs of Figure 6.18 and Figure 6.19. The optimal design results seem to be similar to that in [14]. The iteration converges in about 25 steps and 35 steps on coarse and fine grids respectively. Additionally, the slice of optimal design result at $y = 0.5$ on $32 \times 32 \times 32$ grid and the approximate velocity in the fluid domain are provided in Figure 6.20.

Next, the energy decay properties of the Algorithm 1 with different parameters τ and γ for this problem are shown for the same case of $\bar{\alpha} = 2.5 \times 10^4$ in Figure 6.21. We note that the optimal design results for different parameters τ and γ are similar to that in the left graphs of Figure 6.18 and Figure 6.19. From the two graphs of Figure 6.21, we find that the energy converges to almost the same value when τ or γ is fixed.

Example 6.6. In this example we assume that there are four flow profiles on the inflow boundary and one flow profile on the outflow boundary. The design domain is shown in Figure 6.22. For the four inflow profiles, we let $\bar{g} = 1$, the radius is set as $l = \frac{1}{8}$ and the centers of circles are $(\frac{1}{4}, \frac{1}{4})$, $(\frac{1}{4}, \frac{3}{4})$, $(\frac{3}{4}, \frac{1}{4})$ and $(\frac{3}{4}, \frac{3}{4})$ on the $x = 0$ plane respectively. For the outflow profile, we let $\bar{g} = 1$, $l = \frac{1}{4}$ and $(a, b) = (\frac{1}{2}, \frac{1}{2})$ on the $x = 1$ plane. We set the fluid region fraction as $\beta = \frac{1}{4}$.

We test this problem based on the Algorithm 1 with $\bar{\alpha} = 2.5 \times 10^4$, $\tau = 0.05$, and $\gamma = 0.01$ on $32 \times 32 \times 32$ and $64 \times 64 \times 64$ grids. The initial distribution χ_1 with fluid domain is located in a region of $\{(x, y, z) : x \in$

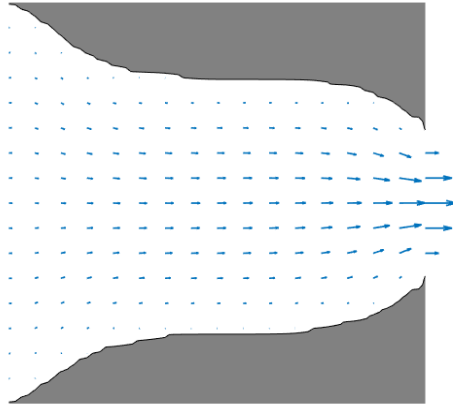


FIGURE 6.20. (Example 6.5) The slice of optimal design result and the approximate velocity in fluid region at $y = 0.5$ on a $32 \times 32 \times 32$ grid. The parameters are set as $\bar{\alpha} = 2.5 \times 10^4$, $\tau = 0.05$, $\gamma = 0.01$.

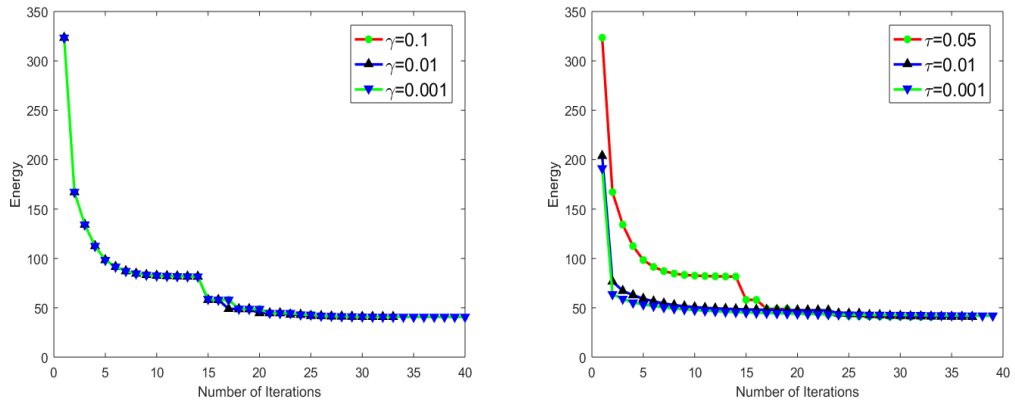


FIGURE 6.21. (Example 6.5) Plot of energy curves for $\bar{\alpha} = 2.5 \times 10^4$ on $32 \times 32 \times 32$ grid. Left: For fixed $\tau = 0.05$, energy curves for the cases of $\gamma = 0.1, 0.01, 0.001$. Right: For fixed $\gamma = 0.01$, energy curves for the cases of $\tau = 0.05, 0.01, 0.001$.

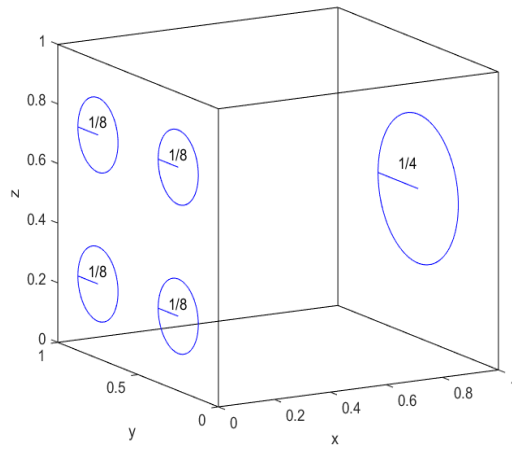


FIGURE 6.22. (Example 6.6) Design domain.

$(0, 1), y \in (0, 1), z \in (\frac{1}{2}, \frac{3}{4})\}$. The corresponding optimal design result is shown in the left graphs of Figure 6.23 and Figure 6.24. From the left graphs of Figure 6.23 and Figure 6.24, we can see that the interface between solid and fluid regions is more smooth when the simulation is performed on the fine grid. From the right graphs of Figure 6.23 and Figure 6.24, the energy decaying property is also observed. The iteration converges in about 50 steps and 70 steps on coarse and fine grids respectively. In Figure 6.25, we present the slice of optimal design result at $z = 25/64$ on a $32 \times 32 \times 32$ grid, and the approximate velocity in the fluid region is also included.

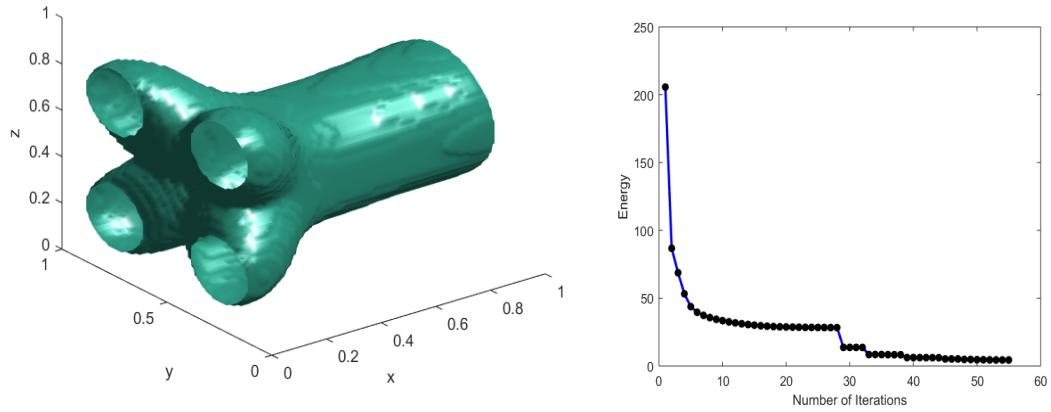


FIGURE 6.23. (Example 6.6) Left: Optimal design result on a $32 \times 32 \times 32$ grid. Right: Energy curve. In this case the parameters are set as $\bar{\alpha} = 2.5 \times 10^4$, $\tau = 0.05$, $\gamma = 0.01$.

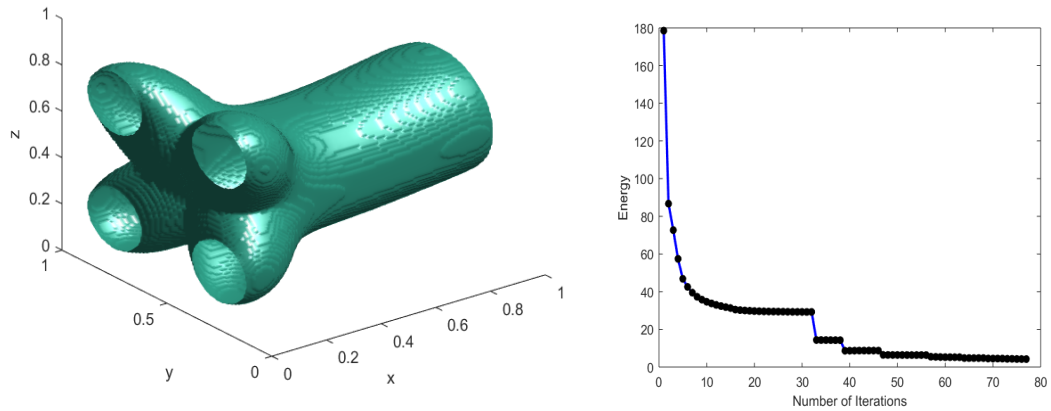


FIGURE 6.24. (Example 6.6) Left: Optimal design result on a $64 \times 64 \times 64$ grid. Right: Energy curve. In this case the parameters are set as $\bar{\alpha} = 2.5 \times 10^4$, $\tau = 0.05$, $\gamma = 0.01$.

6.3. Discussions on the robustness and efficiency of our algorithm. The numerical results in the previous subsections demonstrated the robustness and efficiency of our algorithm. First, the final optimal design result seems to be insensitive to the initial distribution of χ_1 . As shown in the first and second two dimensional examples for the case with $\bar{\alpha} = 2.5 \times 10^4$, even with a random initial distribution of χ_1 , we always get the same final optimal diffuser (cf. Figures 6.2-6.3). From the viewpoint of energy stability, the energy decaying property is proved mathematically and observed numerically for the problem with different initial distributions of χ_1 . Moreover, from the numerical results in Figure 6.4 for the Example 6.1 and Figure

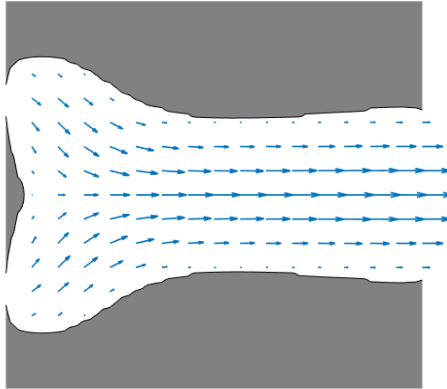


FIGURE 6.25. (Example 6.6) The slice of optimal design result and the approximate velocity in fluid region at $z = 25/64$ on a $32 \times 32 \times 32$ grid. The parameters are set as $\bar{\alpha} = 2.5 \times 10^4$, $\tau = 0.05$, $\gamma = 0.01$.

6.21 for the Example 6.5, we can see that our algorithm is also robust for the different choices of parameters used in the algorithm.

In our algorithm, only a Brinkman problem is solved without the need to solve adjoint problem at each iteration step, and the indicator functions of fluid-solid regions are easily updated based on simple convolutions followed by a thresholding step. Therefore, the computational cost at each iteration is less than that in MMA [12] or in the level set approach [14]. Moreover, our algorithm is much simpler and easier to implement than those methods, and we can also see that our algorithm always converges in few steps.

7. DISCUSSION AND CONCLUSIONS

In this paper, we introduce a new efficient threshold dynamics method for topology optimization for fluids in Stokes flow. We aim to minimize a total energy functional that consists of the dissipation power and the perimeter approximated by nonlocal energy. During the iterations of the algorithm, only a Brinkman equation requires solution by a mixed finite-element method, and the indicator functions of fluid-solid regions are updated by a thresholding step that is based on the convolutions computed by the FFT. A simple adaptive in time strategy is used to accelerate the convergence of the algorithm. The total energy decaying property of the proposed algorithm is rigorously proved and observed numerically. Several numerical examples are tested to verify the efficiency of the new algorithm, and we show that the new algorithm converges more rapidly for most the examples than the MMA used in [12]. Compared to existing methods for topology optimization for fluids, we believe that the proposed algorithm is simple and easy to implement. For the numerical experiments that we have performed thus far, the proposed method always finds an optimal topology and the numerical results are insensitive to the initial guess and parameters. We believe that our algorithm can also be extended to topology optimization for fluids in Navier-Stokes flow.

REFERENCES

- [1] R. Adams, Sobolev Spaces, Academic Press, New York, 1975.
- [2] G. Allaire, F. Jouve, and A. M. Toader, Structural optimization using sensitivity analysis and a level-set method, *Journal of computational physics*, 194(1)(2004), 363-393.
- [3] G. Allaire, C. Dapogny, G. Delgado, and G. Michailidis, Multi-phase structural optimization via a level set method, *ESAIM: control, optimisation and calculus of variations*, 20(2)(2014), 576-611.
- [4] G. Allaire, Optimal design for minimum weight and compliance in plane stress using extrernal microstructures, *Eur. J. Mech. A/Solids* 12 (1993), 839-878.
- [5] G. Allaire and F. Jouve, A level-set method for vibration and multiple loads structural optimization, *Computer methods in applied mechanics and engineering*, 194(30-33)(2005), 3269-3290.
- [6] C. S. Andreasen, A. R. Gersborg, and O. Sigmund, Topology optimization of microfluidic mixers, *Int. J. Numer. Methods Fluids*, 61 (2009), pp. 498–513.
- [7] G. Barles, and C. Georgelin, A simple proof of convergence for an approximation scheme for computing motions by mean curvature, *SIAM J. Numer. Anal.*, 32 (1995), pp. 484–500.
- [8] M. P. Bendsøe. Optimal shape design as a material distribution problem. *Structural optimization*, 1(4):193–202, 1989.

- [9] M. P. Bendsøe and N. Kikuchi, Generating optimal topologies in structural design using a homogenization method, *Comput. Methods Appl. Mech. Eng.*, 71 (1988), pp. 197–224.
- [10] M. P. Bendsøe and O. Sigmund, *Topology Optimization: Theory, Methods and Applications*, Springer, 2003
- [11] E. Bonnetier, E. Bretin, and A. Chambolle, Consistency result for a non monotone scheme for anisotropic mean curvature flow, *Interfaces and Free Boundaries*, 14 (2012), pp. 1–35.
- [12] T. Borrvall and J. Petersson, Topology optimization of fluids in Stokes flow, *Int. J. Numer. Methods Fluids*, 41 (2003), pp. 77–107.
- [13] B. Bourdin and A. Chambolle. Design-dependent loads in topology optimization. *ESAIM: Control, Optimisation and Calculus of Variations*, 9:19–48, 2003.
- [14] V. J. Challis and J. K. Guest, Level set topology optimization of fluids in Stokes flow, *Int. J. Numer. Meth. Engrg.*, 79 (2009), pp. 1284–1308.
- [15] A. Chambolle and M. Novaga, Convergence of an algorithm for the anisotropic and crystalline mean curvature flow, *SIAM J. Math. Anal.*, 37 (2006), pp. 1978–1987.
- [16] H. Chen and X. P. Wang, A one-domain approach for modeling and simulation of free fluid over a porous medium, *J. Comput. Phys.*, 259 (2014), pp. 650–671.
- [17] T. Dbouk, A review about the engineering design of optimal heat transfer systems using topology optimization, *Applied Thermal Engineering*, 112 (2017), pp. 841–854.
- [18] Y. Deng, Z. Liu, P. Zhang, Y. Liu, and Y. Wu, Topology optimization of unsteady incompressible Navier-Stokes flows, *J. Comput. Phys.*, 230 (2011), pp. 6688–6708
- [19] M. B. Duhring, J. S. Jensen, and O. Sigmund, Acoustic design by topology optimization, *J. Sound Vibr.*, 317 (2008), pp. 557–575.
- [20] M. Elsey and S. Esedoğlu, Threshold dynamics for anisotropic surface energies, *Math. Comp.*, 87 (2018), pp. 1721–1756.
- [21] S. Esedoğlu and F. Otto, Threshold dynamics for networks with arbitrary surface tensions, *Comm. Pure Appl. Math.*, 68 (2015), pp. 808–864.
- [22] S. Esedoğlu, S. J. Ruuth, and R. Tsai, Threshold dynamics for high order geometric motions, *Interfaces and Free Boundaries*, 10 (2008), pp. 263–282.
- [23] S. Esedoğlu, Y. H. R. Tsai, Threshold dynamics for the piecewise constant Mumford-Shah functional, *J. Comput. Phys.*, 211 (2006), pp. 367–384.
- [24] L. C. Evans, Convergence of an algorithm for mean curvature motion, *Indiana University Mathematics Journal*, 42 (1993), pp. 533–557.
- [25] H. Garcke, C. Hecht, M. Hinze, and C. Kahle, Numerical approximation of phase field-based shape and topology optimization for fluids, *SIAM J. Sci. Comput.*, 37 (2015), pp. A1846–A1871.
- [26] Y. Van Gennip, N. Guillen, B. Osting and A. L. Bertozzi, Mean curvature, threshold dynamics, and phase field theory on finite graphs, *Milan Journal of Mathematics*, 82 (2014), pp. 3–65.
- [27] A. Gersborg-Hansen, O. Sigmund, and R. Haber, Topology optimization of channel flow problems, *Struct. Multidiscip. Optim.*, 30 (2005), pp. 181–192.
- [28] V. Girault and P. Raviart, *Finite Element Methods for Navier-Stokes Equations: Theory and Algorithms*, Springer-Verlag, Berlin, Heidelberg, New York, 1986.
- [29] E. Giusti, *Minimal Surfaces and Functions of Bounded Variation*, Birkhäuser, Boston, 1984.
- [30] J. K. Guest and J.H. Prévost, Topology optimization of creeping fluid flows using a Darcy-Stokes finite element, *Int. J. Numer. Meth. Engrg.*, 66 (2006), pp. 461–484.
- [31] K. Ishii, Optimal rate of convergence of the Bence–Merriman–Osher Algorithm for motion by mean curvature, *SIAM J. Math. Anal.*, 37 (2005), pp. 841–866.
- [32] M. Jacobs, E. Merkurjev, and S. Esedoğlu, Auction dynamics: A volume constrained MBO scheme, *J. Comput. Phys.*, 354 (2018), pp. 288–310.
- [33] N. Jenkins and K. Maute, Level set topology optimization of stationary fluid-structure interaction problems. *Structural and Multidisciplinary Optimization*, 52(1)(2015), 179-195.
- [34] S. Jiang, D. Wang, and X. P. Wang, An efficient boundary integral scheme for the MBO threshold dynamics method via NUFFT, *J. Sci. Comput.*, 74 (2018), pp. 474–490.
- [35] T. Laux and D. Swartz, Convergence of thresholding schemes incorporating bulk effects, *Interfaces and Free Boundaries*, 19 (2017), pp. 273–304.
- [36] T. Laux and F. Otto, Convergence of the thresholding scheme for multi-phase mean-curvature flow, *Calculus of Variations and Partial Differential Equations*, 55 (2016), p. 129.
- [37] E. Merkurjev, T. Kostic, and A. L. Bertozzi, An MBO scheme on graphs for classification and image processing, *SIAM J. Imaging Sciences*, 6 (2013), pp. 1903–1930.
- [38] B. Merriman, J. K. Bence, and S. Osher, Diffusion generated motion by mean curvature, *UCLA CAM Report 92-18*, 1992.
- [39] B. Merriman, J. K. Bence, and S. Osher, Diffusion generated motion by mean curvature, in *Proceedings of the Geometry Center Workshop*, Minneapolis, MN, 1992.
- [40] B. Merriman, J. K. Bence, and S. Osher, Motion of multiple junctions: A level set approach, *J. Comput. Phys.*, 112 (1994), pp. 334–363.
- [41] B. Merriman and S. J. Ruuth, Convolution-generated motion and generalized Huygens’ principles for interface motion, *SIAM J. Appl. Math.*, 60 (2000), pp. 868–890.
- [42] T. Van Oevelen and M. Baelmans, Numerical topology optimization of heat sinks, *Proceedings of the 15th International Heat Transfer Conference*, 2014, pp. 5985–5999.

- [43] F. Okkels, L. H. Olesen, and H. Bruus, Application of topology optimization in the design of micro and nanofluidic systems, *NSTI-Nanotech* (2005), pp. 575–578.
- [44] F. Okkels, H. Bruus, Scaling behavior of optimally structured catalytic microfluidic reactors, *Phys. Rev. E*, 75 (2007), pp. 1–4.
- [45] L. H. Olesen, F. Okkels, and H. Bruus, A high-level programming-language implementation of topology optimization applied to steady-state Navier-Stokes flow, *Int. J. Numer. Meth. Engrg.*, 65 (2006), pp. 975–1001.
- [46] S. Osher and J. A. Sethian, Fronts propagating with curvature-dependent speed: algorithms based on Hamilton-Jacobi formulations. *Journal of computational physics*, 79(1)(1988), 12-49.
- [47] B. Osting and D. Wang, A generalized MBO diffusion generated motion for orthogonal matrix-valued fields, arXiv preprint arXiv:1711.01365, 2017.
- [48] B. Osting and D. Wang, Diffusion generated methods for denoising target-valued images, arXiv preprint arXiv:1806.06956, 2018.
- [49] R. Picelli, S. Townsend, C. Brampton, J. Norato, H.A. Kim, Stress-based shape and topology optimization with the level set method, *Comput. Methods Appl. Mech. Engrg.*, 329 (2018), pp. 1–23.
- [50] G. Pingen and K. Maute, Optimal design for non-Newtonian flows using a topology optimization approach, *Comput. Math. Appl.*, 59 (2010), pp. 2340–2350.
- [51] A. Takezawa, S. Nishiwaki, and M. Kitamura, Shape and topology optimization based on the phase field method and sensitivity analysis, *J. Comput. Phys.*, 229 (2010), pp. 2697–2718.
- [52] S. J. Ruuth, Efficient algorithms for diffusion-generated motion by mean curvature, *J. Comput. Phys.*, 144 (1998), pp. 603–625.
- [53] S. J. Ruuth, A diffusion-generated approach to multiphase motion, *J. Comput. Phys.*, 145 (1998), pp. 166–192.
- [54] S. J. Ruuth and B. Merriman, Convolution–thresholding methods for interface motion, *J. Comput. Phys.*, 169 (2001), pp. 678–707.
- [55] S. J. Ruuth and B. T. R. Wetton, A simple scheme for volume-preserving motion by mean curvature, *J. Sci. Comput.*, 19 (2003), pp. 373–384.
- [56] O. Sigmund and K. G. Hougaard, Geometric properties of optimal photonic crystals, *Phys. Rev. Lett.*, 100 (2008), 153904.
- [57] O. Sigmund and M. Kurt, Topology optimization approaches. *Structural and Multidisciplinary Optimization*, 48.6 (2013): 1031-1055.
- [58] J. Sokolowski and A. Zochowski. Topological derivative in shape optimization. *Encyclopedia of Optimization*, pages 3908–3918, 2009.
- [59] K. Svanberg, The method of moving asymptotes—a new method for structural optimization, *Int. J. Numer. Meth. Engrg.*, 24 (1987), pp. 359–373.
- [60] D. Swartz and N. K. Yip, Convergence of diffusion generated motion to motion by mean curvature, arXiv preprint arXiv:1703.06519, 2017.
- [61] R. Viertel and B. Osting, An approach to quad meshing based on harmonic cross valued maps and the Ginzburg-Landau theory, arXiv:1708.02316, 2017.
- [62] C. H. Villanueva and K. Maute, CutFEM topology optimization of 3D laminar incompressible flow problems, *Comput. Methods Appl. Mech. Engrg.*, 320 (2017), pp. 444–473.
- [63] X. P. Wang, C. J. Garcia-Cervera, and W. E, A Gauss–Seidel projection method for micromagnetics simulations, *J. Comput. Phys.*, 171 (2001), pp. 357–372.
- [64] D. Wang, H. Li, X. Wei, and X. P. Wang, An efficient iterative thresholding method for image segmentation, *J. Comput. Phys.*, 350 (2017), pp. 657–667.
- [65] D. Wang and B. Osting, A diffusion generated method for computing Dirichlet partitions, arXiv preprint arXiv:1802.02682, 2018.
- [66] D. Wang, X. P. Wang, and X. Xu, An improved threshold dynamics method for wetting on rough surfaces, *J. Comput. Phys.*, 392(2019), pp. 291-310.
- [67] N. Wiker, A. Klarbring, and T. Borrvall, Topology optimization of regions of Darcy and Stokes flow, *Int. J. Numer. Meth. Engrg.*, 69 (2007), pp. 1374–1404.
- [68] Y. Xie, G. Steven, A simple evolutionary procedure for structural optimization. *Computers & Structures*, Dec 3;49(5)(1993):885-96.
- [69] X. Xu, D. Wang, and X. P. Wang, An efficient threshold dynamics method for wetting on rough surfaces, *J. Comput. Phys.*, 330 (2017), pp. 510–528.
- [70] T. Yamada, K. Izui, S. Nishiwaki, and A. Takezawa, A topology optimization method based on the level set method incorporating a fictitious interface energy, *Comput. Methods Appl. Mech. Engrg.*, 199 (2010), pp. 2876–2891.
- [71] V. Young et al., 3D and multiple load case bi-directional evolutionary structural optimization (BESO). *Structural optimization* 18.2-3 (1999): 183-192.
- [72] S. Zhou and Q. Li, A variational level set method for the topology optimization of steady-state Navier-Stokes flow, *J. Comput. Phys.*, 227 (2008), 10178–10195.
- [73] M. Zhou and G. Rozvany. The coc algorithm, part ii: Topological, geometrical and generalized shape optimization. *Computer Methods in Applied Mechanics and Engineering*, 89(1-3):309–336, 1991.

SCHOOL OF MATHEMATICAL SCIENCES AND FUJIAN PROVINCIAL KEY LABORATORY ON MATHEMATICAL MODELING AND HIGH PERFORMANCE SCIENTIFIC COMPUTING, XIAMEN UNIVERSITY, FUJIAN, 361005, CHINA

Email address: `chx@xmu.edu.cn`

DEPARTMENT OF MATHEMATICS, THE HONG KONG UNIVERSITY OF SCIENCE AND TECHNOLOGY, CLEAR WATER BAY, KOWLOON, HONG KONG, CHINA

Email address: `mahtleng@ust.hk`

DEPARTMENT OF MATHEMATICS, UNIVERSITY OF UTAH, SALT LAKE CITY, UTAH, USA

Email address: `dwang@math.utah.edu`

DEPARTMENT OF MATHEMATICS, THE HONG KONG UNIVERSITY OF SCIENCE AND TECHNOLOGY, CLEAR WATER BAY, KOWLOON, HONG KONG, CHINA

Email address: `mawang@ust.hk`